



## OPEN ACCESS

## EDITED BY

Georgios D. Panos,  
Aristotle University of Thessaloniki, Greece

## REVIEWED BY

Lidawani Lambuk,  
Universiti Sains Malaysia, Malaysia  
Satisch Rojekar,  
Icahn School of Medicine at Mount Sinai,  
United States  
Viliana Gugleva,  
Medical University of Varna, Bulgaria  
Velichka Andonova,  
Medical University of Varna, Bulgaria  
Binapani Mahaling,  
Harvard Medical School, United States

## \*CORRESPONDENCE

Élodie Boisselier  
✉ Elodie.Boisselier@fmed.ulaval.ca

RECEIVED 08 January 2025

ACCEPTED 03 March 2025

PUBLISHED 19 March 2025

## CITATION

Raïche-Marcoux G, Méthot S,  
Tchatchouang A, Bettoli C, Maranda C,  
Loiseau A, Proulx S, Rochette PJ, Genin E and  
Boisselier É (2025) Localization of fluorescent  
gold nanoparticles throughout the eye after  
topical administration.  
*Front. Med.* 12:1557611.  
doi: 10.3389/fmed.2025.1557611

## COPYRIGHT

© 2025 Raïche-Marcoux, Méthot,  
Tchatchouang, Bettoli, Maranda, Loiseau,  
Proulx, Rochette, Genin and Boisselier. This is  
an open-access article distributed under the  
terms of the [Creative Commons Attribution  
License \(CC BY\)](https://creativecommons.org/licenses/by/4.0/). The use, distribution or  
reproduction in other forums is permitted,  
provided the original author(s) and the  
copyright owner(s) are credited and that the  
original publication in this journal is cited, in  
accordance with accepted academic  
practice. No use, distribution or reproduction  
is permitted which does not comply with  
these terms.

# Localization of fluorescent gold nanoparticles throughout the eye after topical administration

Gabrielle Raïche-Marcoux<sup>1</sup>, Sébastien Méthot<sup>1</sup>,  
Ange Tchatchouang<sup>1</sup>, Camille Bettoli<sup>2</sup>, Cloé Maranda<sup>1</sup>,  
Alexis Loiseau<sup>1</sup>, Stéphanie Proulx<sup>1</sup>, Patrick J. Rochette<sup>1</sup>,  
Emilie Genin<sup>2</sup> and Élodie Boisselier<sup>1\*</sup>

<sup>1</sup>CHU de Québec Research Center-Université Laval and Department of Ophthalmology and Otolaryngology-Head and Neck Surgery, Faculty of Medicine, Université Laval, Quebec City, QC, Canada, <sup>2</sup>Université de Bordeaux, CNRS, Bordeaux INP, ISM, UMR 5255, Talence, France

The human eye is a highly intricate sensory organ. When a condition requiring treatment occurs, eyedrops, which represent 90% of all ophthalmic treatments, are most frequently used. However, eyedrops are associated with low bioavailability, with less than 0.02% of therapeutic molecules reaching the anterior chamber. Thus, new delivery systems are required to ensure sufficient drug concentration over time at the target site. Gold nanoparticles are a promising avenue for drug delivery; however, they can be difficult to track in biological systems. Fluorescent gold nanoparticles, which have the same ultrastability and biocompatibility as their nonfluorescent counterpart, could act as an effective imaging tool to study their localization throughout the eye after administration. Thus, this study (1) synthesized and characterized fluorescent gold nanoparticles, (2) validated similar properties between nonfluorescent and fluorescent gold nanoparticles, and (3) determined their localization in the eye after topical application on *ex vivo* rabbit eyes. The fluorescent gold nanoparticles were synthesized, characterized, and identified in the cornea, iris, lens, and posterior segment of rabbit eyeballs, demonstrating tremendous potential for future drug delivery research.

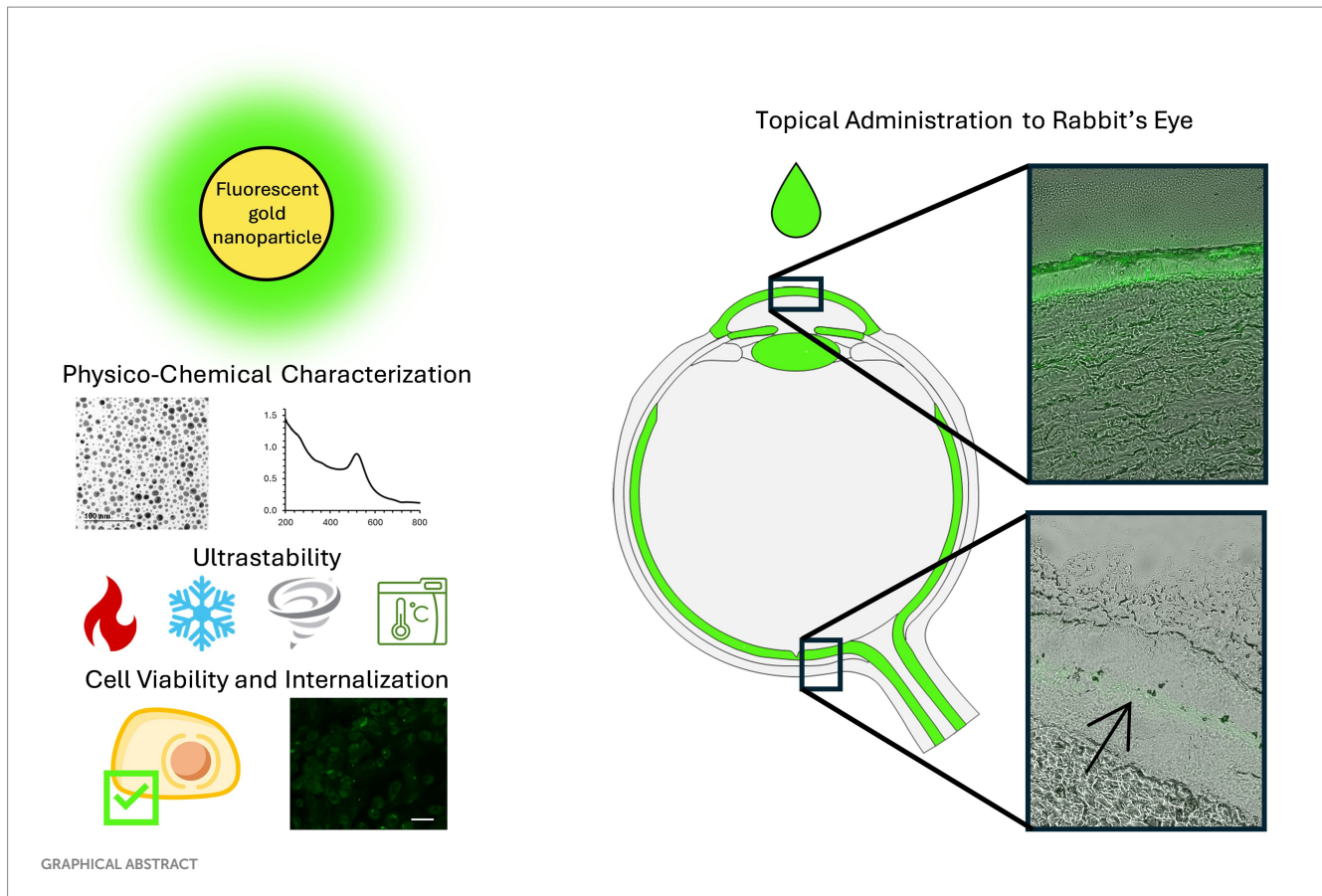
## KEYWORDS

gold nanoparticles, click chemistry, fluorescence imaging, ophthalmology, biodistribution

## 1 Introduction

The eye is one of the most complex and sophisticated sensory organs, and the anatomical structure and physiology of the eye are specifically adapted to allow the passage of light (1). Anatomically, the eye is divided into the anterior and posterior segments, which make up one-third and two-thirds of its total dimension, respectively (2).

The anterior segment encompasses the lacrimal apparatus, cornea, conjunctiva, anterior and posterior chambers, iris, ciliary bodies, lens, and aqueous humor (3). In addition, the anterior segment is very exposed to the environment; thus, it is prone to injuries. The corneal tissue features a complex anatomy that provides significant resistance against the entry of foreign substances and microbes, thereby safeguarding vision (4). Blinking, baseline and reflex tearing, and drainage mechanisms help eliminate harmful microbes, foreign particles, and substances, including drug molecules, from the surface of the eye quickly (5–8). The highly dynamic tear film, which has a renewal rate of 1–3  $\mu\text{L}/\text{min}$  for an overall volume of 3–6  $\mu\text{L}$  for a typical human eye, adds an additional layer of protection (9). In addition, the unique structure of the corneal tear film, with its lipid, aqueous, and



mucoïd layers, impedes the rapid absorption of drug molecules by the corneal epithelial cells (10). Thus, considerable efforts have been directed toward enhancing the permeability and retention time of therapeutic substances on the ocular surface (11). Furthermore, creating drug formulations that require less frequent application will greatly improve patient compliance and overall quality of life (12).

The posterior segment, which includes the sclera, choroid, Bruch's membrane, retina, vitreous humor, and the optic nerve, is vascularized and not easily accessible for noninvasive therapies (13–15). Procedures to control neovascularization in the posterior segment of the eye include laser photocoagulation (16) and photodynamic therapy (17), and, prior to the development of anti-vascular endothelial growth factor (VEGF) therapy, these methods were the standard treatments to prevent further choroidal neovascularization (18, 19). Despite their success, these treatments have limited effects on overall vision, with reports of choroidal neovascularization recurrences and vision loss (20, 21). In addition, these treatments are not suitable for all patients due to varying individual conditions and disease progressions (22). Intravitreal injections of anti-VEGF agents, e.g., ranibizumab (23), bevacizumab (24), and aflibercept (25), are effective in terms of reversing retinal neovascularization. Intravitreal injections increase local drug concentrations in the vitreous chamber; however, they can be painful and require frequent clinic visits and administration by specialists (26). Complications from repeated intravitreal injections can include retinal detachment, hemorrhaging, retinal toxicity, corneal abrasion, temporary elevation of intraocular pressure, and endophthalmitis (27).

Ocular drug administration is crucial for treating common eye diseases, e.g., glaucoma (28), macular degeneration (29), diabetic retinopathy (30), infections (e.g., conjunctivitis, keratitis, and endophthalmitis) (31), and autoimmune disorders (e.g., Sjögren syndrome and uveitis) (32). Each route of ocular administration (topical, intracameral, intravitreal, or periocular) has its advantages and disadvantages. Indeed, intracameral injections bypass pre-corneal barriers, providing high bioavailability for various classes of active molecules. However, potential complications include the toxic effects of active molecules on corneal endothelial cells and toxic anterior segment syndrome (33). Periocular injections (retrobulbar, peribulbar, sub-Tenon, and subconjunctival) are considered less invasive and associated with fewer potential side effects compared to intravitreal injections. However, scleral barriers to the choroid, combined with elimination through blood and lymphatic flow in the subconjunctival space, lead to lower bioavailability in the retina (34). Eyedrops are the most widely used administration pathway, representing 90% of all ophthalmic treatments (35). Eyedrops are noninvasive and can be self-administered, thereby eliminating further doctor visits, which reduces healthcare system congestion. Eyedrops are applied directly to the desired tissue, and systemic administration of therapeutic agents targeting the eye requires high concentrations, which could lead to toxicity (36). The primary disadvantages of eyedrops are the low bioavailability and patient compliance, which reduces the activity of the active molecule (37). Thus, new ocular delivery systems must be developed to ensure that drugs reach the target site in sufficient concentrations over the prescribed period to achieve the desired therapeutic effect.

Drug delivery systems that utilize nanomaterials can play a pivotal role in targeting ocular tissues for treatment. Using such delivery systems offers several advantages, e.g., promoting drug absorption by enhancing their passage through barrier tissues, controlling their release through local administration, and targeting drug action on specific tissues (38, 39). In recent reviews on nanotechnology-based drug delivery systems in ophthalmology, works on biodistribution of micelles, liposomes, dendrimers, nanosuspensions, nanoemulsions and polymeric nanoparticles are mentioned but studies on gold nanoparticles (AuNPs) are often completely omitted (40–48). Among the reviews citing studies on AuNPs in ophthalmology (34, 49–58), the AuNPs are injected intravenously (59–61), intravitreally (62–65), in the subretinal space (66), administered orally (67), used solely *in vitro* (68–72), used on retinal explants (73), loaded onto contact lenses (74–76) or not used for drug-carrying purposes (77–80).

Mucoadhesion, which is the ability to adhere to mucosal tissues, is a leading strategy for topical administration of nanocarriers on the ocular surface (81), and a recent study demonstrated that AuNPs have mucoadhesive properties; thus, AuNPs are promising candidates for drug delivery systems in ophthalmology (82). In addition to their mucoadhesive properties, AuNPs have unique optical characteristics, e.g., surface plasmon resonance (83) that are beneficial for various biomedical applications (84–89). The polyethylene glycol (PEG) modified AuNPs (AuNPs-PEG<sub>2000</sub>) developed in our laboratory are ultrastable (90) and mucoadhesive; thus, they are highly relevant candidates for drug delivery in ophthalmology (91).

To optimize the potential of these patented AuNPs-PEG<sub>2000</sub> (CA3043775) as drug delivery systems, experiments were conducted to better understand their drug loading and drug release properties (92). The next step was an investigation into their behavior and distribution in the eye after topical application. However, they are currently difficult to track with currently available technologies without damaging the biological tissues; thus, we sought to modify them to emit fluorescence without impacting their other properties. This would allow the new fluorescent AuNPs-PEG<sub>2000</sub>-Nap to act as an imaging tool in place of the nonfluorescent AuNPs-PEG<sub>2000</sub>. Therefore, the goal of this study was to (1) synthesize and characterize the fluorescent AuNPs-PEG<sub>2000</sub>-Nap, (2) validate similar properties between the nonfluorescent and fluorescent AuNPs-PEG<sub>2000</sub> and AuNPs-PEG<sub>2000</sub>-Nap, and (3) determine their localization in the eye after topical application using *ex vivo* rabbit eyes. The results of this study are expected to facilitate better understanding of the behavior of the AuNPs-PEG<sub>2000</sub> in physiological conditions and their potential as drug delivery systems in ophthalmology.

## 2 Materials and methods

### 2.1 Materials

Gold chloride trihydrate (HAuCl<sub>4</sub>•3H<sub>2</sub>O), sodium borohydride (NaBH<sub>4</sub>), chlorohydric acid (HCl), nitric acid (HNO<sub>3</sub>), sodium chloride (NaCl), potassium chloride (KCl), sodium phosphate dibasic (Na<sub>2</sub>HPO<sub>4</sub>), potassium phosphate monobasic (KH<sub>2</sub>PO<sub>4</sub>), basic fuchsin (pararosaniline hydrochloride), sodium metabisulfite, isopropanol, and acetonitrile were all purchased from VWR International (Ville Mont-Royal, QC, Canada). Anhydrous copper(II) sulfate (CuSO<sub>4</sub>), ascorbic acid, 4-bromo-1,8-naphthalimide

anhydride, 2-methoxyethylamine, sodium azide, absolute ethanol, petroleum ether, and ethyl acetate were purchased from Sigma-Aldrich (St. Louis, MO, United States). Polyethylene glycol methyl ether thiol with a molecular weight of 2000 g/mol (referred to as HS-PEG<sub>2000</sub>) was purchased from Laysan Bio (Arab, AL, United States). Polyethylene glycol alkyne thiol (referred to as HS-PEG<sub>2000</sub>-ALK) was purchased from Biopharma PEG (Watertown, MA, United States). All glassware used to synthesize the AuNPs was washed thoroughly with aqua regia (3:1 HCl:HNO<sub>3</sub>) and rinsed with nanopure water prior to experimentation. Mucins from the bovine submaxillary gland were purchased from Cedarlane Laboratories (Burlington, ON, Canada). 3-(4,5-dimethylthiazol-2-yl)-5-(3-carboxymethoxyphenyl)-2-(4-sulfophenyl)-2H-tetrazolium (MTS) was obtained from Promega (Madison, WI, United States). Research-grade human eyes were provided by the “Ocular tissue for vision research” infrastructure of the Vision Sciences Research Network, in collaboration with our local eye bank (Banque d’Yeux du Center Universitaire d’Ophtalmologie, Québec, QC, Canada) and Héma-Québec (Québec, QC, Canada) with next of kin consent. This study followed the Declaration of Helsinki and was approved by the CHU de Québec-Université Laval ethics committee (DR-002-955). Eight healthy corneas (age 55–66 years; median 61.5; SD ± 4.6) were used for the characterization of the fluorescence emission, and three (aged 44, 52, and 71 years) were used for hCEC cell isolation and culture, as reported previously (93, 94). Irradiated human fibroblasts (iHFL) were isolated from the foreskin of a 10-day-old donor (95, 96). The OCT compound was obtained from Sakura Finetek (Torrance, CA, United States). Albino rabbit heads (N = 6) were obtained from the Rolland Pouliot & Fils slaughterhouse (Saint-Henri-de-Lévis, QC, Canada).

### 2.2 Synthesis and characterization of 4-azido-N-(2-methoxyethyl)-1,8-naphthalimide

Here, 2-methoxyethylamine (2.59 mL, 29.9 mmol, 2.07 eq) was added to a solution of 4-bromo-1,8-naphthalimide anhydride (4 g, 14.4 mmol, 1 eq) in 50 mL of absolute ethanol. The mixture was refluxed overnight under stirring and then cooled to 0°C by immersing the flask in an ice bath. The solid was collected by filtration to obtain the key intermediate 4-bromo-N-(2-methoxyethyl)-1,8-naphthalimide (4.67 g, 97% yield).

<sup>1</sup>H NMR (300 MHz, CDCl<sub>3</sub>) δ: 8.66 (d, J = 7.3 Hz, 1H, ArH), 8.55 (d, J = 9.0 Hz, 1H, ArH), 8.41 (d, J = 7.8 Hz, 1H, ArH), 8.03 (d, J = 7.8 Hz, 1H, ArH), 7.84 (t, J = 7.6 Hz, 1H, ArH), 4.43 (t, J = 5.8 Hz, 2H, CH<sub>2</sub>), 3.73 (t, J = 5.8 Hz, 2H, CH<sub>2</sub>), 3.37 (s, 3H, CH<sub>3</sub>).

Then, NaN<sub>3</sub> (775 mg, 11.9 mmol, 1.5 eq) was slowly added to a solution of the key intermediate (3 g, 7.95 mmol, 1 eq) in 114 mL of dimethylformamide. The mixture was heated at 70°C under stirring for 2 h. The solvent was removed under reduced pressure. The residue was purified by chromatography on silica gel (petroleum ether/ethyl acetate: gradient from 8:2 to 5:5). 4-azido-N-(2-methoxyethyl)-1,8-naphthalimide was obtained as a pale yellow solid (2.11 g, 84% yield).

<sup>1</sup>H NMR (300 MHz, CDCl<sub>3</sub>) δ: 8.65 (d, J = 7.3 Hz, 1H, ArH), 8.59 (d, J = 7.9 Hz, 1H, ArH), 8.44 (d, J = 8.5 Hz, 1H, ArH), 7.74 (t, J = 7.9 Hz, 1H, ArH), 7.47 (d, J = 7.9 Hz, 1H, ArH), 4.44 (t, J = 5.9 Hz, 2H, CH<sub>2</sub>), 3.73 (t, J = 5.9 Hz, 2H, CH<sub>2</sub>), 3.38 (s, 3H, CH<sub>3</sub>).

The results of the NMR analysis are in agreement with the published values for 4-bromo-N-(2-methoxyethyl)-1,8-naphthalimide and 4-azido-N-(2-methoxyethyl)-1,8-naphthalimide (97). They were recorded using a spectrometer Avance 300 MHz (Bruker). The obtained  $^1\text{H}$  NMR spectra are provided as Supplementary Material (Supplementary Figures 1, 2).

## 2.3 Synthesis of HS-PEG<sub>2000</sub>-nap

In a 25-mL Erlenmeyer flask, 0.02 g of HS-PEG<sub>2000</sub>-ALK (0.005 mmol) was dissolved in 15 mL of acetonitrile. The 4-azido-N-(2-methoxyethyl)-1,8-naphthalimide, 0.0148 g (0.050 mmol) was added to the mixture. Copper sulfate (0.00160 g; 0.005 mmol) and ascorbic acid (0.00176 g; 0.005 mmol) were then added to the Erlenmeyer flask. The mixture was kept at 22°C and shaken using an orbital shaker at 250 rpm overnight in darkness.

## 2.4 Synthesis of AuNPs-PEG<sub>2000</sub>-nap 1%

Stirring at 400 rpm, 250  $\mu\text{L}$  of an aqueous solution of 0.1 g/mL of gold chloride trihydrate (0.06 mmol) was added to 15 mL of a 1:1 acetonitrile:isopropanol mix. 0.0099 g of a HS-PEG<sub>2000</sub> and 750  $\mu\text{L}$  of HS-PEG<sub>2000</sub>-Nap solution obtained previously were added to 30 mL of isopropanol prior to addition to the gold solution. The resulting solution was mixed for 1 h at 400 rpm. While increasing the mixing speed to 700 rpm, a fresh solution of 0.028 g of NaBH<sub>4</sub> (0.74 mmol) in 10 mL of ice-cold water was added dropwise to the gold solution using a peristaltic pump (1 mL/min). The mixture was then stirred at 400 rpm for 3 h to allow the nanoparticles to grow and stabilize in the dark. The solution was evaporated using a rotary evaporator under reduced pressure. Then, 10 mL of water was added to resuspend the nanoparticles. The purification of the nanoparticles performed by dialysis (molecular weight cutoff: 16,000 g/mol) for 7 days, changing the dialysate at least four times per day. After 7 days, the AuNPs-PEG<sub>2000</sub>-Nap 1% were transferred to a polycarbonate centrifuge tube (#355631) and centrifuged with a 70 Ti rotor using the Optima L-90 K Ultracentrifuge from Beckman Coulter Inc. (Indianapolis, IN, United States) at 220,000 g for 18 h. Then, the supernatant was removed and replaced with ultrapure water. The AuNPs-PEG<sub>2000</sub>-Nap 1% were resuspended and moved back to a new dialysis bag with the same molecular weight cutoff for seven supplementary days (dialysates changed four times per day). The AuNPs-PEG<sub>2000</sub>-Nap 1% were then centrifugated again, and the supernatant was changed with ultrapure water. To determine the concentration of the AuNPs in the resultant solution, a known volume of the solution was freeze-dried and weighed ( $n = 3$ ).

## 2.5 Synthesis of AuNPs-PEG<sub>2000</sub>-nap 100%

To obtain AuNPs-PEG<sub>2000</sub>-Nap 100%, 250  $\mu\text{L}$  of an aqueous solution of 0.1 g/mL of gold chloride trihydrate (0.06 mmol) was added to 7.5 mL of the previously synthesized HS-PEG<sub>2000</sub>-Nap and 7.5 mL of isopropanol. All the following steps remain the same as those for the AuNPs-PEG<sub>2000</sub>-Nap 1%.

## 2.6 Characterization of AuNPs-PEG<sub>2000</sub>-nap

### 2.6.1 UV-visible spectroscopy

Here, a quartz cuvette (pathlength: 1 mm  $\times$  10 mm) from Hellma (#104.002-QS) was used (Markham, ON, Canada). The UV-visible spectra were collected from 200 to 800 nm using a Cary Eclipse 50 Bio UV-vis spectrophotometer from Varian (Winnipeg, MB, Canada).

### 2.6.2 First derivative of plasmon band spectra

The UV-visible spectra were normalized using the intensity of the peak of the plasmon band of AuNPs-PEG<sub>2000</sub>-Nap 1% ( $\lambda = 517.5$  nm) and AuNPs-PEG<sub>2000</sub>-Nap 100% ( $\lambda = 519.0$  nm). Then, the data between 430 nm and 630 nm were derived for AuNPs-PEG<sub>2000</sub>-Nap 1% and AuNPs-PEG<sub>2000</sub>-Nap 100%. Here, the inflection point of the derivative was used to determine the position of the plasmon band peak (98–100).

### 2.6.3 Fluorescence spectroscopy

The fluorescence spectra of the AuNPs-PEG<sub>2000</sub>-Nap 1 and 100% samples were obtained using a Fluorolog-3 instrument (Horiba). A 5  $\times$  5 mm light path quartz cuvette from Hellma Analytics was used (#111.057-QS). The excitation wavelength exhibited optimal results at 420 nm; thus, the scans for emission were recorded from 490 to 600 nm.

### 2.6.4 Transmission electron microscopy

Copper grids covered with a vaporized carbon film were purchased from Ted Pella (California, United States). AuNPs-PEG<sub>2000</sub>-Nap 1 and 100% were diluted to a concentration of approximately 0.01 mg/mL, and a 5- $\mu\text{L}$  droplet was deposited on each grid and left to dry overnight. Image acquisition was performed using a JEM 1230 from JEOL Ltd. (Tokyo, Japan). Here, the voltage was set to 80 kV, and a 50,000 $\times$  zoom factor was used. To characterize the size of the gold core, at least 3,000 AuNPs-PEG<sub>2000</sub>-Nap 1% and AuNPs-PEG<sub>2000</sub>-Nap 100% were counted and analyzed for each sample using the ImageJ software.

### 2.6.5 Dynamic light scattering

DLS measurements were performed using the NanoBrook Omni particle analyzer from Brookhaven Instruments Corporation (Holtsville, NY, United States). Each AuNPs-PEG<sub>2000</sub>-Nap was diluted to a concentration of 0.033 mg/mL in PBS (1X). Prior to analysis, the samples were filtered through a 0.2- $\mu\text{m}$  pore size filter. The apparatus was set to an angle of 173° at 25°C. After an equilibrium time of 2 min, 10 measurements of 120 s were performed for each sample. BI-SCP disposable plastic cuvettes from Brookhaven Instruments Corporation (Holtsville, NY, United States) were used for the analysis. The treatment of the size distribution was performed using the CONTIN algorithm.

### 2.6.6 Elemental analysis

Elemental analysis was performed using an ICP-OES, which requires the oxidation of gold prior to analysis. Here, AuNPs-PEG<sub>2000</sub>-Nap 1 and 100% were diluted to a 1:9.5 aqua regia to water ratio and a final AuNP concentration of 0.20 mg/mL. Blank standards containing 5% aqua regia were also analyzed to confirm the absence of contamination specific to the method. The sample preparation was performed in 15-mL tubes from Sarstedt (#62.554.100) (Montreal, QC, Canada). The tubes were heated to 90°C, with care being taken to avoid boiling. The tube caps were left on the tubes and closed by a quarter of a turn. The apparatus used in the experiments was the ICP-OES-5110 (Agilent) in radial mode (Mississauga, ON, Canada).

The calibration methods of the yttrium internal standard and standard addition were performed to prevent matrix effects. Acquisition was achieved at 242.8 nm and 181.9 nm for gold and sulfur quantification, respectively.

## 2.6.7 Molecular weight approximation

The molecular weight (MW) of the AuNPs was determined approximatively following a previously published method (101). Briefly, while assuming monodisperse spherical AuNPs, the volume (V) of the gold core can be estimated as follows.

$$V = \frac{4\pi \times (\text{radius in } \overset{\circ}{\text{A}})^3}{3}$$

The number of gold atoms found in the metallic core, n(Au), can be estimated as follows.

$$n(\text{Au}) = \frac{V \text{ in } \overset{\circ}{\text{A}}^3}{17 \overset{\circ}{\text{A}}^3}$$

With the MW of the Au and S, the number of thiol groups n(S) on the surface can be estimated as follows.

$$\frac{n(\text{Au}) \times \text{MW}(\text{Au})}{\% \text{Au atoms}} = \frac{n(\text{S}) \times \text{MW}(\text{S})}{\% \text{S atoms}}$$

Finally, the MW of AuNPs-Nap 1 and 100% can be estimated using the following equation.

$$\text{MW}(\text{AuNPs} - \text{PEG}_{2000} - \text{Nap } 1\%) = [n(\text{Au}) \times \text{MW}(\text{Au})] + 0.01[n(\text{S}) \times (\text{MW}(\text{PEG} - \text{Nap}))] + 0.99[n(\text{S}) \times \text{MW}(\text{PEG})]$$

$$\text{MW}(\text{AuNPs} - \text{PEG}_{2000} - \text{Nap } 100\%) = [n(\text{Au}) \times \text{MW}(\text{Au})] + 0.01[n(\text{S}) \times (\text{MW}(\text{PEG} - \text{Nap}))]$$

## 2.6.8 Graft density approximation

The graft density  $\rho_g$  was determined using the calculated number of ligands n(S) used in the approximation of the MW. The surface of the metallic core A, assuming monodisperse spherical nanoparticles, can be calculated as follows.

$$A = 4\pi \times (\text{radius in nm})^2$$

Thus, the graft density can be evaluated as follows.

$$\rho_g = \frac{n(\text{S})}{A}$$

## 2.7 Biolocalization in human corneas

The human corneas were rinsed with PBS to remove the storing liquid and placed on a small support (epithelium side up). A punched out 6-mm diameter rubber stencil was centered on the cornea to ensure that the deposited drop remained on the cornea and did not flow over and to the side after application. A drop (50  $\mu\text{L}$ , 1 mg/mL) of AuNPs-PEG<sub>2000</sub>, AuNPs-PEG<sub>2000</sub>-Nap 1%, and AuNPs-PEG<sub>2000</sub>-Nap 100% were placed on top of the corneas. Then, the corneas were placed in the dark for 2 h before being prepared for tissue imaging.

## 2.8 Ultrastability assays

The protocol used to qualify the ultrastability properties strictly followed the previously established protocol (90).

## 2.9 Quantification of mucoadhesion

The protocol used to quantify the adsorbed mucins on the surface of the AuNPs strictly followed a previously published PAS coloration protocol (101).

## 2.10 MTS assays

MTS viability assay was performed according to the manufacturer's instructions (Promega, Madison, WI). Briefly, hCECs ( $1 \times 10^4$ ) in corneal epithelium medium [Dulbecco–Vogt modification of Eagle's medium (Gibco, Waltham, MA, United States) with Ham's F12 (3:1) (Life Technologies, Carlsbad, CA, United States), supplemented with 5% FetalClone II serum (HyClone, Logan, UT, United States), 5  $\mu\text{g}/\text{mL}$  insulin (SAFC Bioscience, Lenexa, KS, United States), 0.4  $\mu\text{g}/\text{mL}$  hydrocortisone (Teva, Toronto, ON, Canada), 10 ng/mL epidermal growth factor (R&D Systems, Oakville, ON, Canada),  $10^{-10}$  mol/L cholera toxin (Sigma-Aldrich, St. Louis, MO, USA), 100  $\mu\text{g}/\text{mL}$  Penicillin (Fresenius Kabi, Homburg, Germany), and 25  $\mu\text{g}/\text{mL}$  Gentamycin (Galenova, Saint-Hyacinthe, QC, Canada)] and incubated at 37°C for 4 h prior to the addition of AuNPs (AuNPs-PEG<sub>2000</sub> and AuNPs-PEG<sub>2000</sub>-Nap 1%, at concentrations of 0, 0.001, 0.1, 0.25, 0.50, 0.75 and 1.00  $\mu\text{M}$ ). After 18 h, MTS (2 mg/mL) was added to each well, and the plates were incubated at 37°C for 1 h. Then, the optical density (OD) was measured using a microplate reader (Biorad Model 550, Mississauga, ON, Canada) at a wavelength of 490 nm. OD of the blank solution (AuNPs, no cells) was subtracted, and results presented relative to the control (0  $\mu\text{M}$  AuNPs, which represents 100% viability). Experiments were performed using 3 different cell populations, in triplicate.

## 2.11 Internalization assays

hCECs ( $0.3 \times 10^6$  cells) were plated directly in six-well plates (9.6  $\text{cm}^2$ ) in the corneal epithelium medium described above. Before the cells reached confluence, AuNPs-PEG<sub>2000</sub> and AuNPs-PEG<sub>2000</sub>-Nap 1% (500  $\mu\text{L}$ , 1 mg/mL, diluted with PBS) were added. After a waiting time of 30 min, the cells were rinsed with PBS before

image acquisition was performed using an Axio Imager Z2 Upright Microscope (Carl Zeiss, North York, ON, Canada).

## 2.12 Biolocalization with rabbit eyes

The rabbit eyeballs were removed from the skull and placed on a small support (cornea side up). A 20-mm diameter rubber gasket well was centered on the cornea to ensure that the deposited drop remained on the cornea and did not flow onto the globe after application. A drop (50  $\mu$ L, 1 mg/mL) of AuNPs-PEG<sub>2000</sub>-Nap 1% was placed in the middle of the stencil. Here, two waiting times were tested, i.e., 2 h [to maximize the interactions mucins-AuNPs, as previously demonstrated (101)] and 3 min ( $n = 3$  eyes per condition). For the 2-h waiting time, the eyeballs were placed in the dark before the drop was applied. After 2 h, the globes were prepared for imaging. For the 3-min waiting time, which mimics the renewal rate of the tear film (9), the eyeballs were washed thoroughly with PBS to ensure that no AuNPs-PEG<sub>2000</sub>-Nap 1% remained on the ocular surface. The eyeballs were then placed in the dark for 2 h for comparison with the first waiting time before tissue preparation for imaging. The controls ( $n = 3$  eyes) received a drop of PBS and were placed in the dark for 2 h prior to tissue preparation.

## 2.13 Tissue preparation for imaging

The dissections were performed to separate the corneas, irises, lenses, and posterior segment of the eyes, and to avoid all cross-contamination. The centers of all corneas were cut using a 6-mm biopsy punch before being placed (endothelium down) in an OCT compound from Sakura Finetek (Torrance, CA, United States). The cut samples were then stored at 80°C at least overnight before making cuts using a cryostat microtome (Leica, Concord, Canada). The irises were placed flat with the posterior epithelium down in the OCT compound, and the lens was placed with the epithelium side up. A portion of the posterior segment was removed using a 10-mm biopsy punch to facilitate manipulation. The punched sample was put in the OCT compound. All samples were stored at 80°C at least overnight before making microtome cryostat cuts. Prior to being placed on microscope slides, the samples of the corneas (human and rabbit), iris, and posterior segments were sliced (thickness: 8  $\mu$ m), and the lens samples were prepared with a thickness of 16  $\mu$ m. Upon microscopic examination, samples without AuNPs were used to determine the exposure time that prevented the background signal and endogenous fluorescence in the sample.

## 3 Results and discussion

The development of effective delivery systems relies heavily on optimizing formulation and process parameters and thoroughly characterizing the physicochemical and biological properties of nanocarriers. In ocular drug delivery, key factors to assess include particle size and distribution, surface charges, encapsulation efficiency, drug loading capacity, drug release profiles, uptake mechanisms, stability, and safety or toxicity (102). Additionally, the delivery system must meet specific ocular requirements such as sterility, osmolality, pH, surface tension, and viscosity to ensure compatibility and efficacy. Important properties, like particle size and polydispersity index, are

critical for the physical stability of nanocarriers. For ocular formulations, particles larger than 10  $\mu$ m are generally unsuitable (103). Smaller, monodisperse particles are preferred for their enhanced stability, biodistribution (104), and reduced risks of instability issues like sedimentation during storage (105). Their small size facilitates faster penetration into the tear film's mucin layer, reduces irritation, and enhances uptake by corneal epithelial cells (106). While smaller nanoparticles show greater absorption into the aqueous humor, they are cleared more quickly from tear fluid (107). The shape and surface morphology of nanoparticles also influence their biodistribution, cellular uptake, and toxicity. Spherical nanoparticles are generally more effective in enhancing drug performance compared to other shapes like cubes or rods (108). Surface modifications are also important factors for biodistribution: different polymeric nanoparticles, and even different polymeric shells will have different biodistribution profiles in the anterior and posterior segment (109, 110).

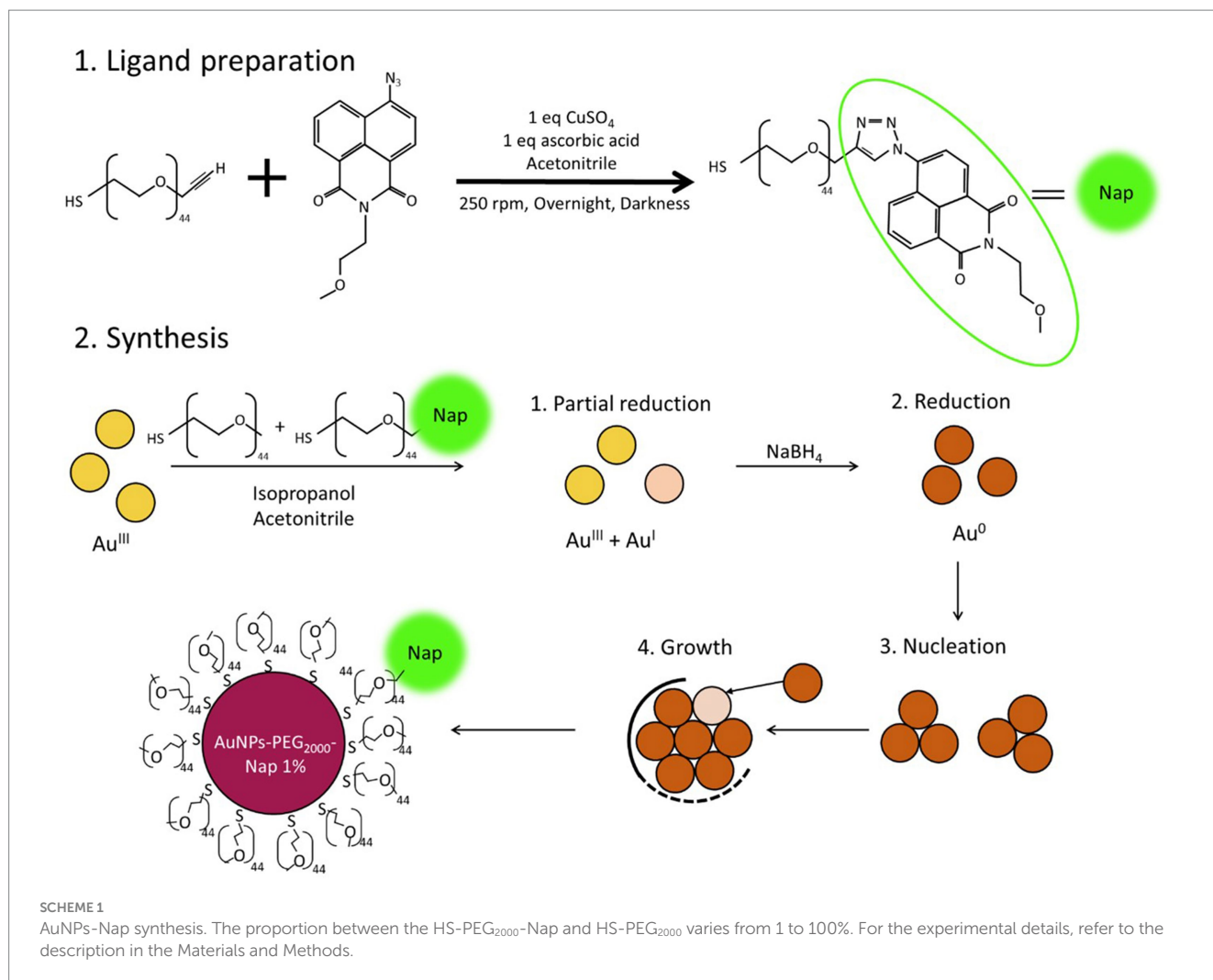
To investigate the localization of nonfluorescent AuNPs after eyedrop application, a strategy was required to determine their trajectory accurately. As previously synthesized, the gold core combined into the PEGylated ligands created a furtive drug delivery system (111, 112); thus, the goal was to minimally modify the AuNPs-PEG2000, that are small, spherical, stable and biocompatible, to generate an imaging tool that would be visible in microscopy and replicate the nonfluorescent AuNPs-PEG2000 behavior. Here, fluorescence microscopy was selected for its sensitivity (113), its compatibility with animal and human tissues (114), and the minimal modification required to the AuNPs-PEG2000 to make them fluorescent (115, 116). Once the characteristics of the AuNPs-PEG2000 and fluorescent AuNPs-PEG2000-Nap were determined to be equivalent, internalization assays were conducted prior to performing biolocalization experiments.

## 3.1 Synthesis and physicochemical characterization of fluorescent AuNPs

### 3.1.1 Synthesis of fluorescent AuNPs-PEG<sub>2000</sub>-nap

To obtain AuNPs-PEG<sub>2000</sub>-Nap, the first step involved synthesizing the fluorescent ligand (HS-PEG<sub>2000</sub>-Nap; Scheme 1). Here, a heterobifunctional PEGylated ligand (HS-PEG<sub>2000</sub>-ALK), with an alkyne functional group on one end (dedicated to the click reaction) and a thiol group (-SH) on the other, was employed to covalently bond the naphthalimide (Nap) fluorophore and coordinate with the Au atoms of the core (through the thiol group). The click reaction (117) was performed with stoichiometric equivalents of reagents, and the azido-naphthalimide equivalent was 10 times the molar equivalent of the ligand. The advantage of this molecule lies in its difference in fluorescence emission before and after the click reaction (118). In fact, prior to the click reaction, the azido-naphthalimide was very weakly fluorescent, whereas it became a strong fluorophore after the formation of the triazole heterocycle.

Here, the synthesis process was a modified version of the Brust-Schiffrin synthesis (119) based on specific experimental conditions leading to small ultrastable AuNPs (90). Two types of AuNPs-PEG<sub>2000</sub>-Nap were obtained with this synthesis, i.e., AuNPs-PEG<sub>2000</sub>-Nap 1% and AuNPs-PEG<sub>2000</sub>-Nap 100%, where 1 and 100% of the ligands used for the synthesis were the HS-PEG<sub>2000</sub>-Nap,



respectively. For the AuNPs-PEG<sub>2000</sub>-Nap 1%, the remaining 99% of the ligands were monofunctional HS-PEG<sub>2000</sub> (90). Once the fluorescent HS-PEG<sub>2000</sub>-Nap was obtained, it was added in different proportions in the synthesis of the AuNPs. Mixing the PEGylated ligands with chloroauric acid (HAuCl<sub>4</sub>) caused a partial reduction of the Au atoms. Note that the success of this synthesis is dependent on the balance between the crystal growth and the ligand capping speeds, i.e., if the crystal growth outpaces the ligand capping speed, the particles will not stabilize properly and will precipitate. In addition, acetonitrile in the reaction mixture slows the crystal growth because its nitrogen atoms partially stabilize the Au core growth. Furthermore, NaBH<sub>4</sub> exhibits lower reducing strength in acetonitrile compared to water, which further slows the crystal growth. This slower growth allows for better capping and results in more stable AuNPs (120).

Prior to characterization, the synthesis was purified via dialysis and precipitation by ultracentrifugation to further change the dialysate (refer to the Materials and Methods).

### 3.1.2 Physicochemical characterization of AuNPs-PEG<sub>2000</sub>-nap 1 and 100%

The UV-visible spectra showed that the surface plasmon resonance absorbance peaks for AuNPs-PEG<sub>2000</sub>-Nap 1% and

AuNPs-PEG<sub>2000</sub>-Nap 100% are centered at 517.5 nm and 519.0 nm, respectively (Table 1). In addition, the elemental analysis via ICP-OES revealed varying weight percentages of gold and sulfur in the AuNPs. Here, AuNPs-PEG<sub>2000</sub>-Nap 1% contained 48.5% gold and 0.41% sulfur, and AuNPs-PEG<sub>2000</sub>-Nap 100% contained 62.5% gold and 0.67% sulfur (Table 1). The TEM observations showed that the gold core diameters were  $6.0 \pm 3.0$  nm and  $4.8 \pm 2.4$  nm for the AuNPs-PEG<sub>2000</sub>-Nap 1% and AuNPs-PEG<sub>2000</sub>-Nap 100%, respectively (Table 1). Based on the metallic core diameters and elemental compositions, the molecular weights were calculated to be 2,002, 334 g/mol for AuNPs-PEG<sub>2000</sub>-Nap 1% and 1,185,970 g/mol for AuNPs-PEG<sub>2000</sub>-Nap 100% (Table 1). DLS measurements showed hydrodynamic diameters of  $29 \pm 1$  nm for AuNPs-PEG<sub>2000</sub>-Nap 1% and  $34.0 \pm 0.6$  nm for AuNPs-PEG<sub>2000</sub>-Nap 100% (Table 1). In addition, the graft density for AuNPs-PEG<sub>2000</sub>-Nap 1% was 3.05 ligands per nm<sup>2</sup> of gold core, and that for the AuNPs-PEG<sub>2000</sub>-Nap 100% was 3.10 ligands per nm<sup>2</sup> of gold core (Table 1).

The core diameter and number of ligands were the highest for AuNPs-PEG<sub>2000</sub>-Nap 1%, and the percentage of sulfur atoms was the lowest, which can be attributed to the varying behavior of the AuNPs based on their molecular weights, especially during the stabilization of the gold core. In water, PEG alone can adopt Gaussian coil or flat plate configurations (121), and it stabilizes molecules or proteins with

TABLE 1 Characterization of AuNPs-PEG<sub>2000</sub>-Nap 1% and AuNPs-PEG<sub>2000</sub>-Nap 100%.

	AuNPs-PEG <sub>2000</sub> -Nap 1%	AuNPs-PEG <sub>2000</sub> -Nap 100%
Position of plasmon band peak (nm) <sup>a</sup>	517.5	519.0
% Au atoms <sup>b</sup>	48.5	62.5
% S atoms <sup>b</sup>	0.41	0.67
Core diameter (nm) <sup>c</sup>	6.0 ± 3.0	4.8 ± 2.4
Hydrodynamic diameter (nm) <sup>d</sup>	29 ± 1	34.0 ± 0.6
Number of ligands <sup>e</sup>	345	224
Molecular weight (g/mol) <sup>f</sup>	2,002,334	1,185,970
Graft density (number of ligand/nm <sup>2</sup> ) <sup>f</sup>	3.05	3.10

<sup>a</sup>The position of the plasmon band peak was obtained using ultraviolet (UV)-visible spectroscopy.

<sup>b</sup>% Au and S atoms were determined by elemental analysis using inductively coupled plasma optical emission spectroscopy (ICP-OES).

<sup>c</sup>The core diameters were determined by transmission electron microscopy (TEM).

<sup>d</sup>The hydrodynamic diameters were determined by dynamic light scattering (DLS).

<sup>e</sup>The number of ligands was calculated per AuNPs-PEG<sub>2000</sub>-Nap.

<sup>f</sup>The molecular weights and graft density were calculated theoretically. Experimental and calculation details are described in the Materials and Methods Section.

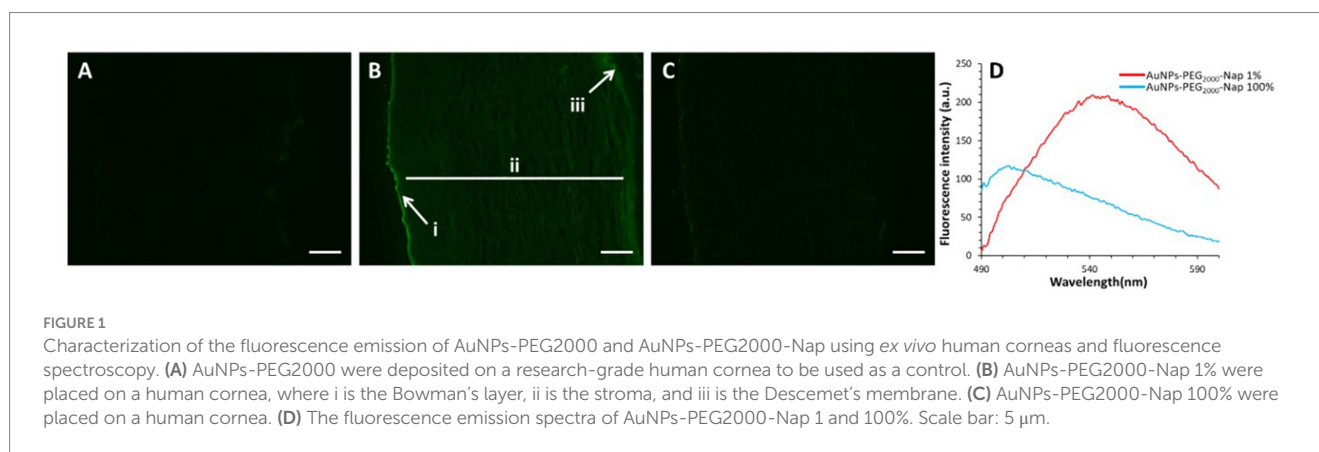


FIGURE 1

Characterization of the fluorescence emission of AuNPs-PEG<sub>2000</sub> and AuNPs-PEG<sub>2000</sub>-Nap using *ex vivo* human corneas and fluorescence spectroscopy. (A) AuNPs-PEG<sub>2000</sub> were deposited on a research-grade human cornea to be used as a control. (B) AuNPs-PEG<sub>2000</sub>-Nap 1% were placed on a human cornea, where i is the Bowman's layer, ii is the stroma, and iii is the Descemet's membrane. (C) AuNPs-PEG<sub>2000</sub>-Nap 100% were placed on a human cornea. (D) The fluorescence emission spectra of AuNPs-PEG<sub>2000</sub>-Nap 1 and 100%. Scale bar: 5  $\mu$ m.

wrapped or expanded configurations (122). During AuNPs-PEG<sub>2000</sub>-Nap growth (refer to Scheme 1), the utilization of these two types of PEG (HS-PEG<sub>2000</sub>-Nap and HS-PEG<sub>2000</sub>) in different proportions can lead to different behaviors, resulting in the core diameters ranging from 6.0 ± 3.0 nm to 4.8 ± 2.4 nm, which are still quite similar on the nanometer scale. It is likely that HS-PEG<sub>2000</sub>-Nap experiences more steric hindrance, thereby reducing the thiol group's ability to reach the gold core. This steric hindrance may also enhance stabilization, producing smaller cores than expected. Consequently, the smaller gold core of AuNPs-PEG<sub>2000</sub>-Nap 100% leads to a smaller number of stabilizing ligands around the nanoparticles, thereby making AuNPs-PEG<sub>2000</sub>-Nap 1% have the largest gold core diameter and number of ligands. With the largest core diameter, AuNPs-PEG<sub>2000</sub>-Nap 1% contained 6,652 gold atoms, which is significantly more than the AuNPs-PEG<sub>2000</sub>-Nap 100%, which had 3,406 gold atoms. However, for AuNPs-PEG<sub>2000</sub>-Nap 1%, this only represents 0.41% by mass despite having 345 sulfur atoms. The graft density showed very similar numbers of ligands per nm<sup>2</sup> of gold core surface for both AuNPs-PEG<sub>2000</sub>-Nap 1 and 100%, i.e., 3.05 and 3.10 ligands/nm<sup>2</sup>, respectively.

Continuing the physical characterization of AuNPs-PEG<sub>2000</sub>-Nap 1 and 100%, the fluorescence emission of the nanoparticles was tested with *ex vivo* human corneas (Figure 1) to identify the best AuNPs-PEG<sub>2000</sub>-Nap for colocalization experiments. A drop (50  $\mu$ L, 1 mg/mL)

of AuNPs-PEG<sub>2000</sub> (Figure 1A), AuNPs-PEG<sub>2000</sub>-Nap 1% (Figure 1B), and AuNPs-PEG<sub>2000</sub>-Nap 100% (Figure 1C) was deposited on the top of the human corneas and incubated at room temperature for 2 h before being prepared for image acquisition (Materials and Methods). The fluorescence emission spectra of AuNPs-PEG<sub>2000</sub>-Nap 1% and AuNPs-PEG<sub>2000</sub>-Nap 100% (Figure 1D) were also obtained in water. The AuNPs-PEG<sub>2000</sub>-Nap 1% ( $\lambda_{\text{max, emission}} = 544$  nm) had the highest fluorescence emission intensity and was the most visible in the cornea. In fact, AuNPs-PEG<sub>2000</sub>-Nap 1% could be found in the Bowman's layer, throughout the entire stroma and the Descemet's membrane, with a stronger affinity with the Bowman's layer. For AuNPs-PEG<sub>2000</sub>-Nap 100% ( $\lambda_{\text{max, emission}} = 503$  nm), the fluorescence was less discernible in the cornea than with AuNPs-PEG<sub>2000</sub>-Nap 1%. The difference in the fluorescence emission spectra could hypothetically come from the difference in the steric hindrance between AuNPs-PEG<sub>2000</sub>-Nap 1% and AuNPs-PEG<sub>2000</sub>-Nap 100% (123). The presence of Nap groups on all 224 PEGylated ligands of AuNPs-PEG<sub>2000</sub>-Nap 100% could cause steric hindrance, thereby not permitting the Nap group free rotations and reducing the extent of the intramolecular charge transfer, which could explain the blue shift observed in the fluorescence spectra (Figure 1D) (124, 125). The difference in the emission intensities is likely due to aggregation-caused quenching. For the AuNPs-PEG<sub>2000</sub>-Nap 100%, the aromatic Nap fluorophores are closer and can give rise to intermolecular



interactions, e.g.,  $\pi$ - $\pi$  stacking, which commonly results in reduced fluorescence (126). Between the two fluorescent AuNPs-PEG<sub>2000</sub>-Nap 1 and 100%, the AuNPs-PEG<sub>2000</sub>-Nap 1% appear to present better fluorescent properties for further physiological experiments. The AuNPs-PEG<sub>2000</sub>-Nap could potentially benefit from fine-tuning experiments to investigate the number of Nap groups required to realize optimal fluorescence while modifying the other AuNP properties minimally.

## 3.2 Biological properties of AuNPs-PEG2000-nap

With the goal of using AuNPs-PEG2000 as ocular drug delivery systems, these nanoobjects must exhibit several critical biological properties, e.g., ultrastability under conditions mimicking formulation steps and the physiological environment, mucoadhesion, and biocompatibility. The following three sections describe the biological properties of the AuNPs and their behavior in the presence of human corneal epithelial cells (hCEC).

### 3.2.1 Ultrastability

Frequently, the weak colloidal stability of AuNPs excludes their utilization in specific fields (127). For example, instability in physiological buffering salts restricts the utilization of many types of nanoparticles for biomedical applications [e.g., drug delivery (128), gene therapy (129), biosensing (130), and imaging (131)] because blood is a rich and highly ionic media (132). In addition, for nanoparticles, the loss of colloidal stability can result in precipitation, reshaping, corrosion, and, most importantly, the loss of key physicochemical properties like delivery, optoelectronic, biocompatibility, biodegradability, magnetic, or catalytic abilities (133). Thus, it is crucial to preserve the original size, shape, structure, composition, and aggregation state of the nanoparticles in biological environments for the required duration to achieve the intended use (134). This preservation is essential for maintaining the functionality of nanoparticles and preventing undesired effects (135). Given that nonfluorescent AuNPs-PEG<sub>2000</sub> can withstand harsh conditions (90), e.g., several cycles of freeze-drying, heating, ultracentrifugation, and autoclave sterilization, the goal was to verify that the fluorescent AuNPs-PEG<sub>2000</sub>-Nap 1 and 100% would support the same conditions. In this study, their colloidal stability was assessed using different methodologies, including UV-visible spectroscopy, DLS, and TEM (Table 2).

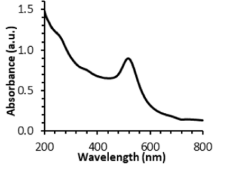
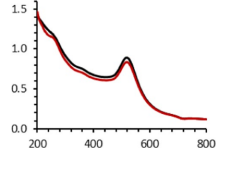
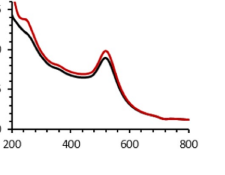
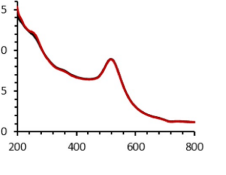
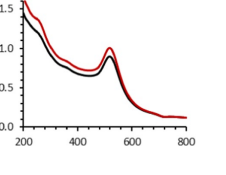
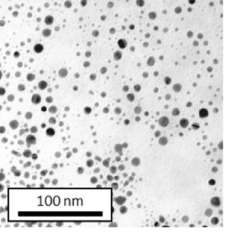
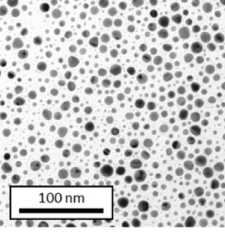
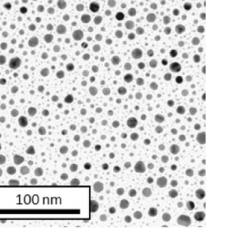
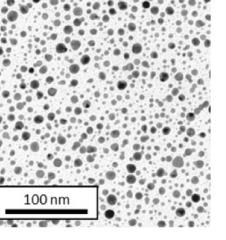
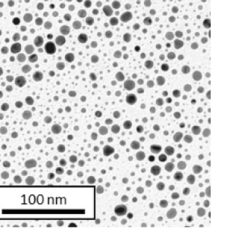
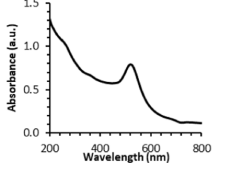
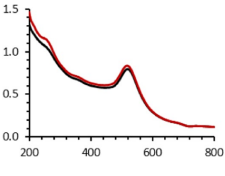
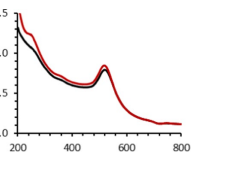
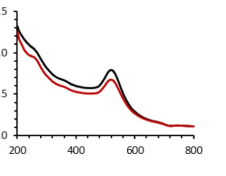
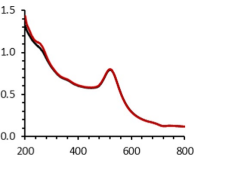
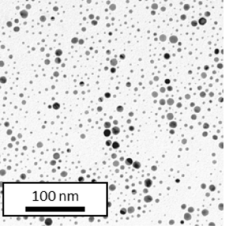
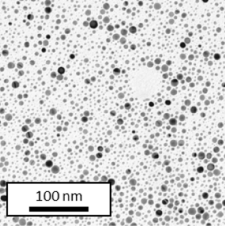
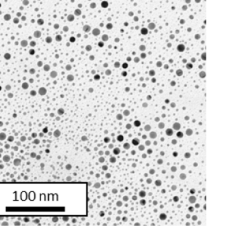
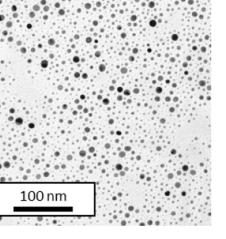
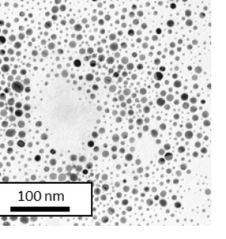
An interesting characteristic of AuNPs is the ability of the conduction electrons of the gold atoms to oscillate coherently when irradiated by the oscillating electric field of light. The localized surface plasmon resonance (LSPR) effect causes an absorbance band in the electromagnetic spectrum, typically in the visible light range. The absorption peak can be altered by variations in different factors, e.g., the particle size and shape, coating, the distance between particles, pH, temperature, the number and types of the ligands linked to the gold core, and the surrounding physicochemical environment (136, 137). Here, the plasmonic band shift, which was measured accurately with the first derivative, was used to determine the colloidal stability of AuNPs-PEG<sub>2000</sub>-Nap 1 and 100% to different treatments (Supplementary Figure 3) (98). The colloidal stability results for AuNPs-PEG<sub>2000</sub>-Nap 1 and 100% are shown in Table 2.

The UV-visible spectra were obtained with 0.050 mg/mL of AuNPs-PEG<sub>2000</sub>-Nap 1 and 100% before and after three cycles of 24-h freeze-drying, three periods of 12-h heating at 65°C, and three precipitations by ultracentrifugation, and sterilization using an autoclave (Table 2). Tables 2A,B show the colloidal stability results for AuNPs-PEG<sub>2000</sub>-Nap 1% and AuNPs-PEG<sub>2000</sub>-Nap 100%, respectively. As can be seen, the UV-visible spectrum for each AuNP-PEG<sub>2000</sub>-Nap observed after treatment, represented by the full red lines, is nearly the same as the initial spectrum, represented by the full black lines. The LSPR position of AuNPs-PEG<sub>2000</sub>-Nap 1% before and after all treatments, which was determined by calculating the derivative of the spectra, remained at 517.5 nm (Supplementary Figure 1). For AuNPs-PEG<sub>2000</sub>-Nap 100%, the derivative of the plasmon bands exhibited a slight shift, translating into a disturbance of the gold core. Specifically, only the sterilization caused a 0.75 nm shift of the plasmon band peak of AuNPs-PEG<sub>2000</sub>-Nap 1%, and it caused a 2.00 nm shift for AuNPs-PEG<sub>2000</sub>-Nap 100% (Supplementary Figure 4).

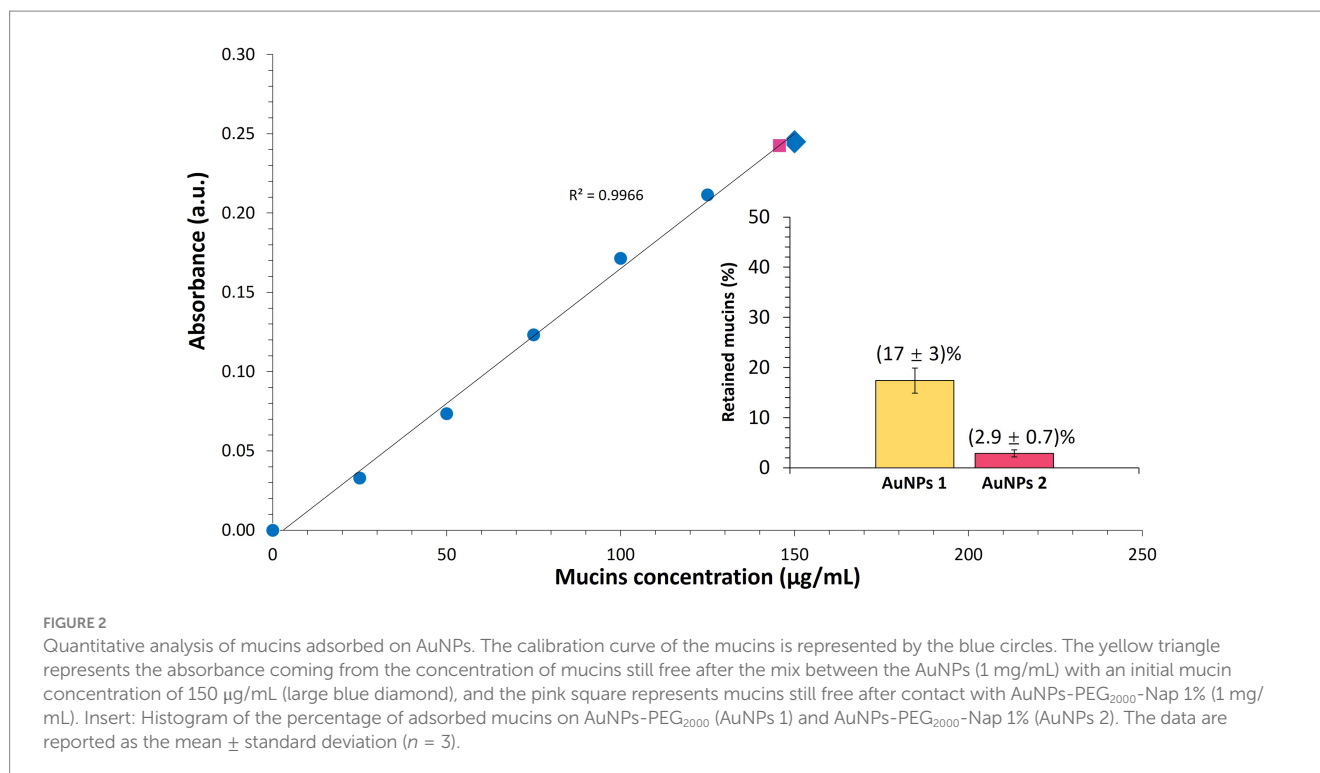
AuNPs-PEG<sub>2000</sub>-Nap 1% were able to sustain the ultrastability testing as very small variations in the UV-visible spectra, the TEM images, and the hydrodynamic diameters can be observed. AuNPs-PEG<sub>2000</sub>-Nap 100% also exhibited little variation in the physicochemical parameters after freeze-drying, centrifugation, sterilization, and heating. In addition, the plasmon bands observed in the UV-visible spectroscopy remained similar with no variations in the observed plasmon band peak position. However, a slight increase in the intensity of the entire spectrum of AuNPs-PEG<sub>2000</sub>-Nap 1% was observed after sterilization and heating, which is likely due to the evaporation of a small part of the total volume. For AuNPs-PEG<sub>2000</sub>-Nap 100%, a slight reduction in the global intensity was observed after centrifugation, which suggests that some of the AuNPs-PEG<sub>2000</sub>-Nap 100% could aggregate during this step. The mean core of the diameter of AuNPs-PEG<sub>2000</sub>-Nap 1 and 100%, extracted from TEM images using the ImageJ software, did not vary significantly after each treatment (Table 2). The DLS experiments yielded quite similar results after all treatments and showed no signs of aggregation for AuNPs-PEG<sub>2000</sub>-Nap 1%. However, the same cannot be said for AuNPs-PEG<sub>2000</sub>-Nap 100%. Here, the hydrodynamic diameter varied significantly depending on the treatment, especially after freeze-drying (from  $34.0 \pm 0.6$  nm to  $332 \pm 74$  nm, as shown in Table 2B). The increased number of Nap groups appeared to alter the colloidal stability, thereby leading to a likely agglomeration in the solution. Note that a detectable level of fluorescence was maintained after all treatments for both AuNPs (Supplementary Figure 5).

To the best of our knowledge, the ultrastable AuNPs-PEG<sub>2000</sub>-Nap 1% are the first reported fluorescent AuNPs that can sustain autoclave sterilization without major changes in their UV-visible spectra and both the core and hydrodynamic diameters, as previously showcased with their nonfluorescent counterpart (90). As mentioned previously, colloidal stability is essential to preserve the functionality of AuNPs-PEG<sub>2000</sub> and AuNPs-PEG<sub>2000</sub>-Nap, especially if AuNPs-PEG<sub>2000</sub> are used as a drug delivery system for topically applied treatments (102). The results of the physical characterization suggest that AuNPs-PEG<sub>2000</sub>-Nap 1% could be a promising candidate as an imaging tool for AuNPs-PEG<sub>2000</sub>. Combined with the ultrastability assay, the previous fluorescence experiments (Figure 1) have both shown that AuNPs-PEG<sub>2000</sub>-Nap 1% is the most suitable fluorescent probe for imaging purposes while offering the same

TABLE 2 Ultrastability characterization of (A) AuNPs-PEG<sub>2000</sub>-Nap 1% and (B) AuNPs-PEG<sub>2000</sub>-Nap 100% before treatment and after three cycles of 24-h freeze-drying, sterilization by an autoclave, three precipitations by ultracentrifugation, and three periods of 12-h heating at 65°C.

A	Before	Freeze-drying	Sterilization	Centrifugation	Heat
UV-visible					
TEM (diameter)	 (6.0 ± 3.0) nm	 (6.4 ± 2.4) nm	 (8.2 ± 3.0) nm	 (5.4 ± 3.0) nm	 (6.2 ± 2.8) nm
DLS (diameter)	(29.0 ± 1.0) nm	(28.6 ± 0.6) nm	(27.8 ± 0.4) nm	(26.8 ± 0.8) nm	(28.0 ± 0.6) nm
B	Before	Freeze-drying	Sterilization	Centrifugation	Heat
UV-visible					
TEM (diameter)	 (4.8 ± 2.4) nm	 (4.0 ± 2.6) nm	 (4.8 ± 2.6) nm	 (4.2 ± 2.4) nm	 (4.6 ± 2.4) nm
DLS (diameter)	(34.0 ± 0.6) nm	(332 ± 74) nm	(37.4 ± 1.6) nm	(42.2 ± 1.6) nm	(39.4 ± 1.8) nm

The UV-visible spectra of the AuNPs-PEG<sub>2000</sub>-Nap before and after the different treatments are represented by the solid black and solid red lines, respectively. The core diameters and hydrodynamic diameters were obtained from the TEM images and DLS, respectively. The experimental details are given in the Materials and Methods.



properties as the nonfluorescent AuNPs-PEG<sub>2000</sub> (90). Thus, we focus on AuNPs-PEG<sub>2000</sub>-Nap 1% in all subsequent experiments.

### 3.2.2 Mucoadhesion

Various techniques have been developed to study mucoadhesion in order to quantify and characterize how different materials interact with mucins (81, 138, 139). Mucins are glycoproteins found in the airways, gastrointestinal tract, genitourinary tract, nasal cavity, mouth, throat, and ocular surface (140). As the bottom layer of the tear film, the mucoid layer on the ocular surface is responsible for the maintenance of the lacrimal fluid, lubrication to facilitate blinking, ensuring a smooth surface for vision, and protection by trapping and removing pathogens and debris (141). Mucoadhesive drug delivery systems can increase their residence time in the precorneal film, which could broaden the drug release window and potentially reduce the required number of eyedrop applications (142).

A protocol adapted for AuNPs mucoadhesion involves the periodic acid/Schiff's reagent (PAS) coloration method (143). This method analyzes the mucin content and mucoadhesion by oxidizing saccharide hydroxyl groups and reacting them with decolorized fuchsin, resulting in a color change that is detectable by UV-visible spectroscopy (144). A protocol has been perfected and optimized for its combination with AuNPs, in consideration of their high visible light absorbance (108).

The nonfluorescent AuNPs-PEG<sub>2000</sub> could adsorb  $11 \pm 4\%$  of the 150 µg of mucins they were incubated with, and the AuNPs-PEG<sub>2000</sub>-Nap 1% were able to retain  $2.9 \pm 0.7\%$  of the same initial amount of mucins (Figure 2). AuNPs can exhibit mucoadhesive properties due to their ability to bind to mucins through two main mechanisms, i.e., (1) the formation of S-S bonds with the thiol groups at the metallic core and (2) the direct interaction of the cysteine groups with the gold core via Au-S bonds. The presence of some

peripheral Nap groups on AuNPs-PEG<sub>2000</sub>-Nap 1% could account for the observed differences compared with conventional AuNPs-PEG<sub>2000</sub>. When mucins attempt to interact near the core, the steric hindrance from the Nap groups may prevent the access of many proteins. In addition, the very high graft density (3.05 ligands/nm<sup>2</sup>) of PEGylated ligands on AuNPs-PEG<sub>2000</sub>-Nap 1% could contribute to the high motility in mucus (145). In fact, the AuNPs-PEG<sub>2000</sub> and AuNPs-PEG<sub>2000</sub>-Nap 1% exhibited low percentages of adsorbed mucins; however, their high graft density could increase the diffusion into the mucous layer. This could potentially increase the residence time of the drug delivery systems, which would increase the local concentrations of therapeutic molecules near the corneal epithelial cells.

### 3.2.3 Cytotoxicity

In a previous paper, MTS viability assays with different types of AuNPs, including AuNPs-PEG<sub>2000</sub>, were performed at low AuNP concentrations (from 0.0005 to 0.406 µM) (90), and showed a high cell viability for all concentrations tested. Herein, a MTS viability assay was conducted to determine if the addition of the Nap group to the AuNPs-PEG<sub>2000</sub> could impact cell viability. We also increased the range of AuNP concentrations to evaluate the highest concentration that could affect cell viability. Results for each AuNP concentration and type (Figure 3) show a similar viability between the AuNPs-PEG<sub>2000</sub> and the AuNPs-PEG<sub>2000</sub>-Nap 1% for all the concentrations tested, meaning that fluorescent molecules covalently bonded to PEG do not impact biological response differently than the non-fluorescent ones (only descriptive statistics were used). Furthermore, results show that concentrations between 0.0001 and 0.75 µM AuNPs had a cell viability similar to the control (no AuNPs), and only a  $9 \pm 14\%$  and a  $22 \pm 28\%$  cell death was observed for the highest concentration of AuNPs (1 µM) for, respectively, the AuNPs-PEG<sub>2000</sub> and the AuNPs-PEG<sub>2000</sub>-Nap 1%. These results indicate that AuNPs-PEG<sub>2000</sub>-Nap 1%

are adequate for fluorescent biolocalization studies and biodistribution experiments.

### 3.2.4 Cell internalization

Finally, prior to performing *ex vivo* localization experiments, AuNPs-PEG<sub>2000</sub> and AuNPs-PEG<sub>2000</sub>-Nap 1% were placed into wells of hCECs for 30 min to gather data on possible AuNPs internalization into the cells. After incubation for 30 min, the wells were rinsed with a phosphate-buffered saline (PBS) wash and then observed under an epifluorescence microscope using the fluorescein isothiocyanate (FITC) filters. The results indicate that some hCECs exhibit a small degree of autofluorescence in the same wavelength range as the AuNPs-PEG<sub>2000</sub>-Nap 1% emission (Figure 4A). However, the distinction between this background fluorescence and the emitted fluorescence coming from AuNPs-PEG<sub>2000</sub>-Nap 1% observed in Figure 4 is obvious because the cells are clearly visible in Figure 4B compared with Figure 4A. In addition, this assay confirmed that AuNPs-PEG<sub>2000</sub>-Nap 1% are internalized into hCECs because fluorescence can be observed in the cytoplasm and is absent in the nucleus. If the AuNPs-PEG<sub>2000</sub>-Nap 1% had covered the surface of the cell without penetrating the cells, the fluorescence would have been

uniform, and a distinction between the cytoplasm and nucleus would not be observable.

Thus, the AuNPs-PEG<sub>2000</sub>-Nap 1% emit strong fluorescence with minimal change to the original nonfluorescent AuNPs-PEG<sub>2000</sub> by simply adding a fluorescent probe to 1% of their attached PEGylated ligands (approximately 3–4 Nap groups per gold core). In addition, they exhibit the same ultrastability properties as the AuNPs-PEG<sub>2000</sub>, i.e., they can sustain rigorous conditions without significantly impacting the plasmon band position, the colloidal stability measured by DLS, and the gold core diameter measured using TEM images. Furthermore, compared to the AuNPs-PEG<sub>2000</sub>, addition of the PEG<sub>2000</sub>-Nap 1% did not reduce cell viability, as shown by the results of the MTS assay (Figure 3). Combined, these similarities demonstrate that AuNPs-PEG<sub>2000</sub>-Nap 1% can be utilized as a substitute for AuNPs-PEG<sub>2000</sub> to study their biodistribution and biolocalization.

### 3.3 Biolocalization study using AuNPs-PEG<sub>2000</sub>-nap 1%

A significant challenge in clinical translation lies in the lack of animal models that accurately replicate the human ocular system's anatomy and physiology. Rodents are commonly used for safety and efficacy evaluations due to their cost-effectiveness and ease of handling. However, the extrapolation of pharmacodynamic responses from rodents to humans can be unreliable due to significantly different anatomy (146). Compared to rodents, rabbits exhibit greater anatomical and physiological similarities to humans, particularly regarding eye size, vitreous humor volume, and internal structure, providing a comparable pathway for topically administered compounds (147). Nevertheless, key differences remain, such as the higher viscosity of rabbit aqueous humor, larger anterior chambers, and greater blinking frequency, which must be carefully considered (148). In this study, *ex vivo* rabbit eyeballs were used, thereby eliminating significant factors impacting biodistribution and elimination of topically applied nanoparticles, such as tear film dynamics, blinking and systemic circulation (149, 150). Whole eyeballs from slaughterhouse rabbits were used in the biolocalization experiments. Here, a drop (50  $\mu$ L, 1 mg/mL) of AuNPs-PEG<sub>2000</sub>-Nap 1% diluted in PBS was placed on the cornea for each eyeball. The application time was either 3 min to replicate the renewal

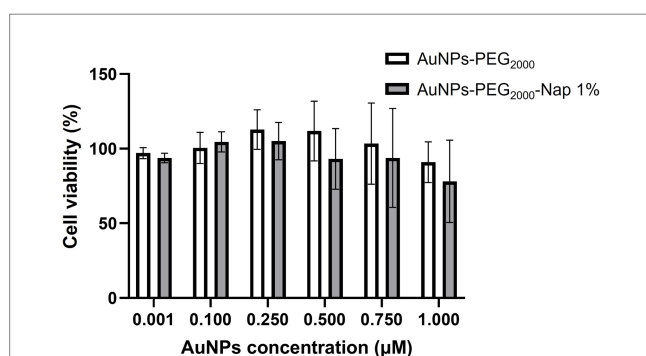


**FIGURE 3**  
Effect AuNPs-PEG<sub>2000</sub> and AuNPs-PEG<sub>2000</sub>-Nap 1% on cell viability. The hCECs were cultured as monolayers (10,000 cells per well, three wells per condition, repeated using three different populations) and exposed to increasing doses of AuNPs-PEG<sub>2000</sub> and AuNPs-PEG<sub>2000</sub>-Nap 1% for 18 h. Cell viability was assessed using an MTS assay. Results are presented as mean  $\pm$  standard deviation.

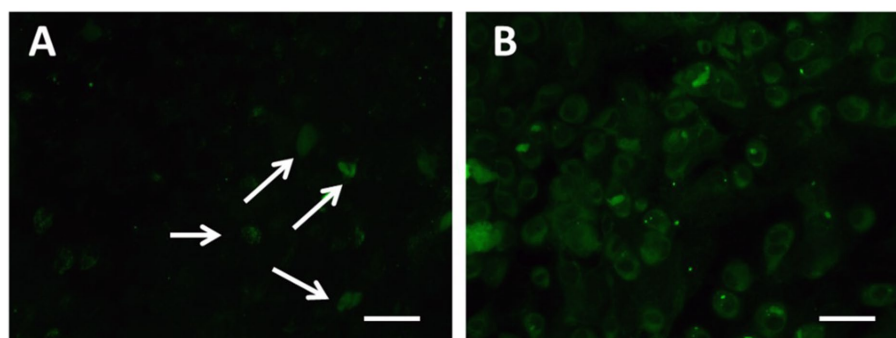
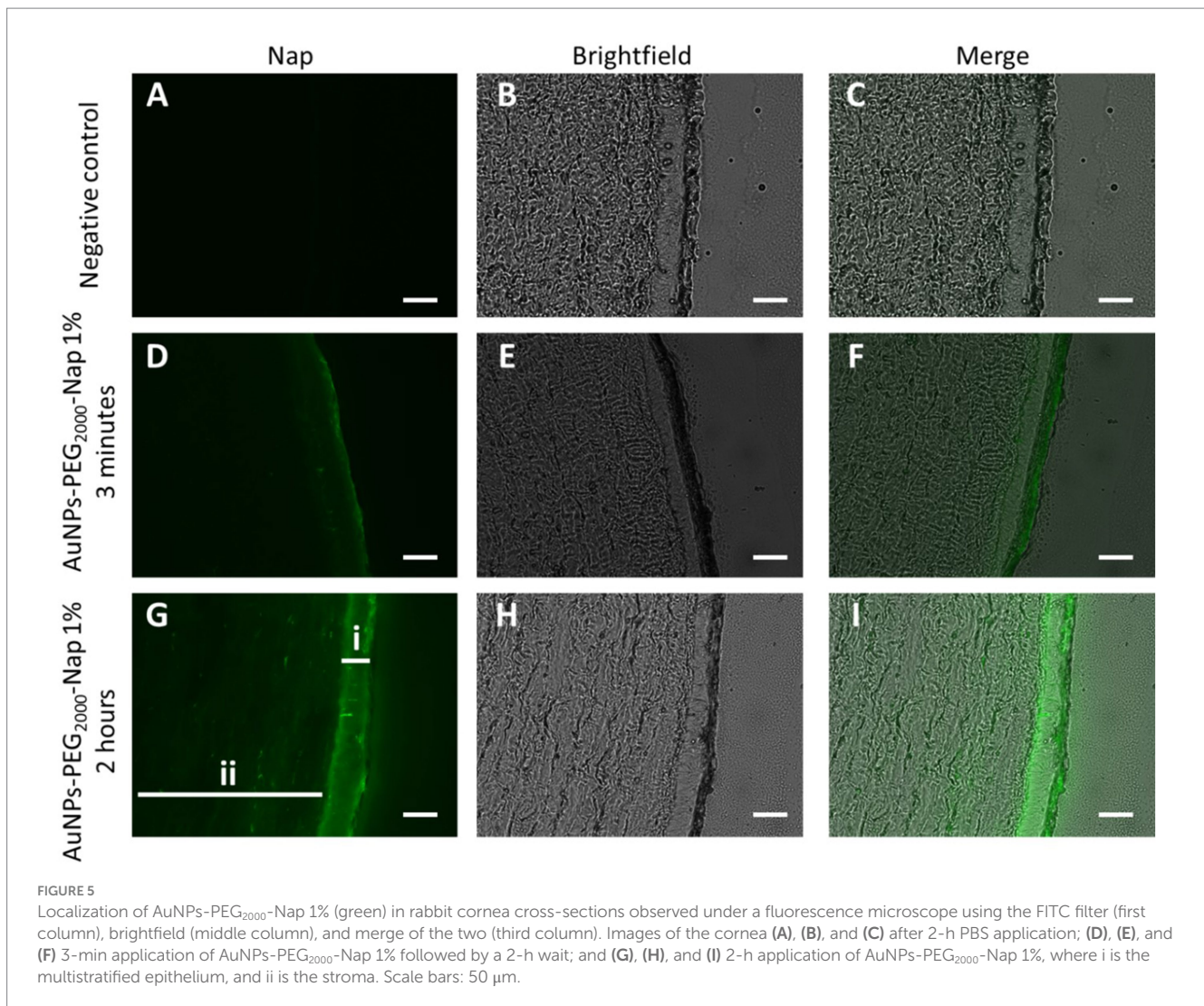


**FIGURE 4**  
Fluorescence assay of internalized of (A) control AuNPs-PEG<sub>2000</sub> and (B) AuNPs-PEG<sub>2000</sub>-Nap 1% (green) by cultured hCECs with FITC filters. The arrows point to hCECs slightly showing autofluorescence. Scale bars: 10  $\mu$ m.



rate of the tear film (9) or 2 h to increase the interaction probability with the tear film and their diffusion. In addition, the corneas, irises, lenses and posterior segments were dissected carefully to avoid contamination between the different ocular tissues and then embedded in an optimum cutting temperature (OCT) compound and cut at the cryostat. No fixation steps were carried out before microscopy in order to avoid any physicochemical modification of the eye tissues that could impact the localization of AuNPs-PEG<sub>2000</sub>-Nap 1%. Therefore, this method provides a more direct way to observe the biodistribution of gold nanoparticles in the different structures of the eye (151).

### 3.3.1 Cornea

The human cornea comprises three cellular layers (i.e., the epithelium, stroma, and endothelium) and two acellular layers that separate them (i.e., Bowman's layer and Descemet's membrane) (152).

AuNPs-PEG<sub>2000</sub>-Nap 1% were found in the cornea for both application times (Figure 5). Note that more AuNPs-PEG<sub>2000</sub>-Nap 1% were found in the corneal epithelium after 2 h, as the epithelial layer was more defined, clearly observable, and brighter, as shown in Figure 5G. The 3-min application was sufficient for AuNPs-PEG<sub>2000</sub>-Nap 1% to adhere

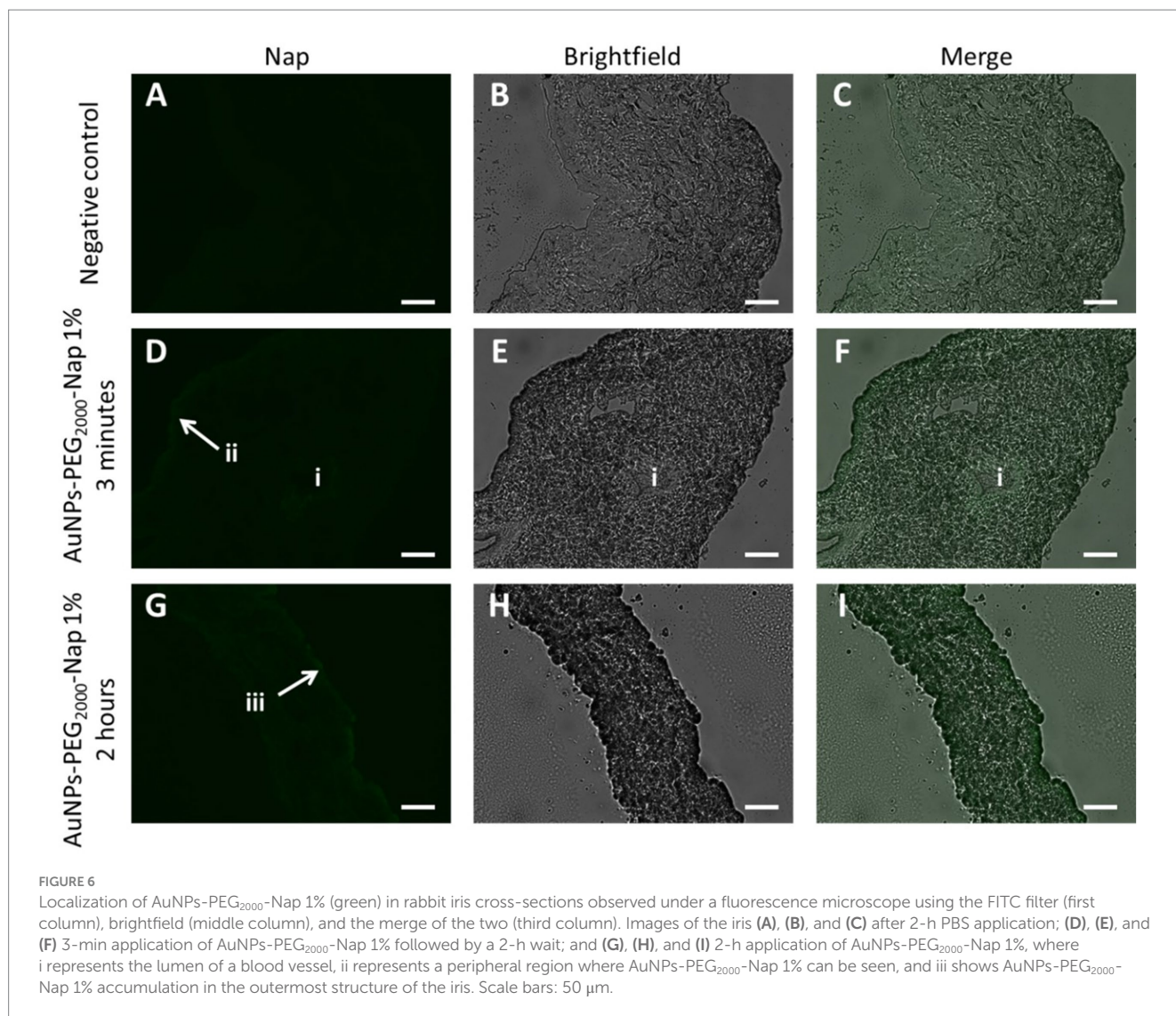
to the ocular surface because fluorescence can be observed in the corneal epithelium (Figure 5D) even after the vigorous PBS wash. Fluorescent AuNPs-PEG<sub>2000</sub>-Nap 1% were also found in the stroma for both application times, which means that the AuNPs-PEG<sub>2000</sub>-Nap 1% were not confined to the direct application site or the corneal epithelium, benefiting motility by their high graft density. In addition, there appeared to be an affinity between AuNPs-PEG<sub>2000</sub>-Nap 1% and the corneal epithelium because the brightness levels between the epithelial layer and the stroma present a clear intensity difference, especially after 2 h.

The AuNPs-PEG<sub>2000</sub>-Nap 1% are not the first AuNPs to be topically applied and found in the corneal epithelium and stroma (77, 79, 80) but they are the only PEGylated AuNPs synthesized from a one-pot synthesis.

### 3.3.2 Iris

The iris plays a crucial role in visual function by regulating the amount of light entering the eye and reaching the retina (153). The iris also participates in the circulation of aqueous humor, thereby helping to regulate the intraocular pressure (154).

Fluorescence can be faintly observed in the Nap images (Figure 6) without any clear preference for an iris structure. For the image obtained after the 3-min application, the lumen of a blood vessel was visible, in addition to the outermost periphery of the



structure (Figure 6D), and AuNPs-PEG<sub>2000</sub>-Nap 1% can be observed in the extremity of the iris for the 2-h application (Figure 6G).

Note that the experiments were conducted using eyes from albino rabbits, which possess no pigment; thus, the iris pigment epithelium and the pigmented anterior surface were difficult to identify. However, AuNPs-PEG<sub>2000</sub>-Nap 1% had a strong affinity with the corneal epithelium (Figure 5); thus, we can expect to find AuNPs in similar cell types in other tissues, e.g., the epithelium of the iris. Nevertheless, it is important to underline that it is impossible to discern with certitude the exact iris structure in which the AuNPs-PEG<sub>2000</sub>-Nap 1% were found, only that they were found in the iris after only a 3-min application.

### 3.3.3 Lens

The lens, which is an elastic and transparent biconvex structure located in the posterior chamber, comprises four parts, i.e., the lens capsule, epithelial cells, lens fibers, and zonules (155).

As shown in Figure 7, AuNPs-PEG<sub>2000</sub>-Nap 1% were observed in the anterior part of the lens after the 3-min application. In fact, the fluorescent probe accumulated slightly in the epithelial cell monolayer of the lens (Figure 7C). Note that the epithelium of the lens is only

located on its anterior part. In the images of the posterior part of the lens (Figures 7G,L), no AuNPs-PEG<sub>2000</sub>-Nap 1% can be observed. Knowing this, the possibility of the AuNPs-PEG<sub>2000</sub>-Nap 1% being in the lens capsule rather than the lens epithelium is excluded because fluorescence would be visible on the posterior part of the lens. The same tendencies were observed for the 2-h application.

To conclude on the distribution of the AuNPs in the anterior segment of the eye, the AuNPs-Nap 1% were readily observed in the corneal epithelium, the iris, potentially in its pigment epithelium, and in the lens epithelium. The fluorescent probe successfully crossed the anterior part of the rabbits' eyeballs; however, most of the fluorescence was observed in the cornea.

### 3.3.4 Posterior segment

In these experiments, the sampled posterior segment comprised the retina, choroid, and sclera. The retina, which is located in the posterior part of the eye, is a transparent, light-sensitive tissue composed of multiple cellular layers (156). The retina includes the light-transducing neural retina and the retinal pigment epithelium (RPE) (157). The neural retina is a layered structure comprising six major types of neurons organized into three nuclear layers containing

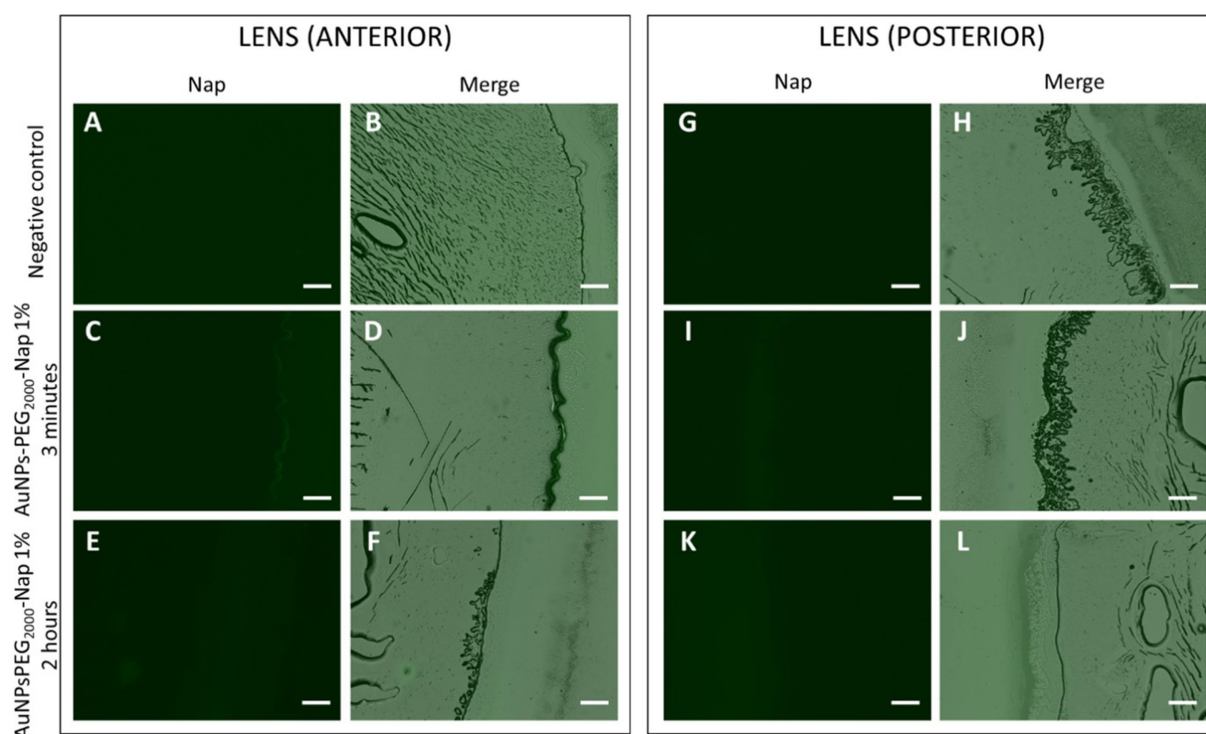


FIGURE 7

Localization of AuNPs-PEG<sub>2000</sub>-Nap 1% (green) in the rabbit lens cross-sections observed under a fluorescence microscope using the FITC filter (first column) and the merge of the brightfield and FITC filter (second column) divided in two parts, where the anterior segment is closest to the cornea, and the posterior segment is closest to the back of the eye. Images of the anterior part of the lens (A) and (B) after 2-h PBS application; (C) and (D) 3-min application of AuNPs-PEG<sub>2000</sub>-Nap 1% followed by a 2-h wait; and (E) and (F) 2-h application of AuNPs-PEG<sub>2000</sub>-Nap 1%; (G) and (H) images of the posterior part of the lens after 2-h PBS application; (I) and (J) 3-min application of AuNPs-PEG<sub>2000</sub>-Nap 1% followed by a 2-h wait, and (K) and (L) 2-h application of AuNPs-PEG<sub>2000</sub>-Nap 1%. Scale bar: 50  $\mu$ m.

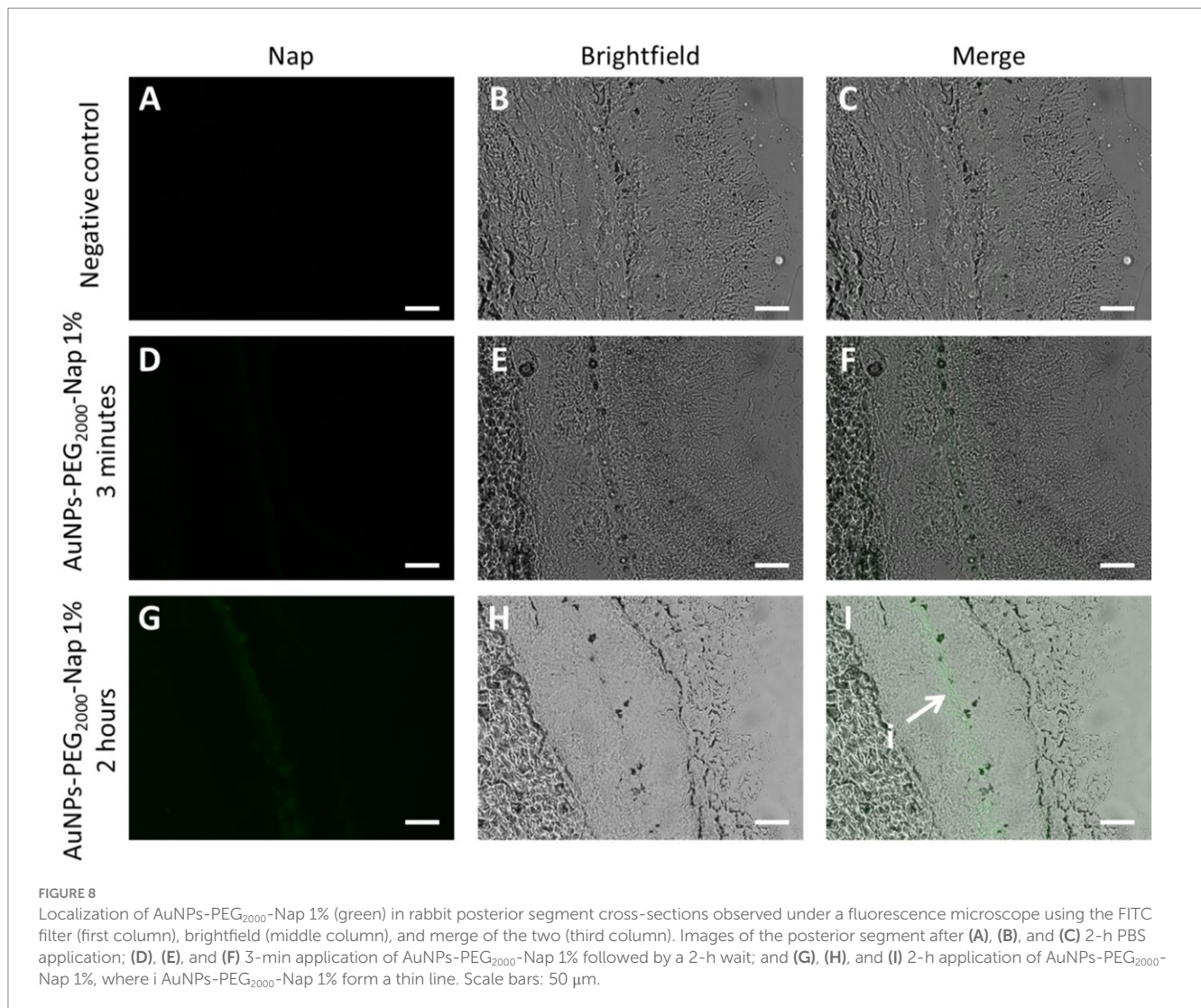
neuronal cell bodies (or somas) and two plexiform layers where synapses occur (158).

Experimentally, a sample of the back of the eyeball was taken using a 10-mm diameter biopsy punch to facilitate manipulations. Here, the three-layering tissues, i.e., the retina, choroid, and sclera, were kept together. The AuNPs-PEG<sub>2000</sub>-Nap 1% were found in the posterior segment of the eye, as shown in Figure 8. For both application times, the AuNPs-PEG<sub>2000</sub>-Nap 1% were organized in a thin line in a specific structure of the retina; however, due to the lack of melanin pigment in albino rabbits, it is difficult to distinguish exactly where the choroid ends and the retina begins, thereby making it difficult to precisely identify the tissue sublayers where the AuNPs-PEG<sub>2000</sub>-Nap 1% are found. However, we did not expect to find them there because the AuNPs-PEG<sub>2000</sub>-Nap 1% had to go through the vitreous humor to migrate from the lens to the retina. The vitreous humor is a viscoelastic extracellular matrix hydrogel with a water content between 98 and 99.7% (159). The findings of this study demonstrate that the AuNPs-PEG<sub>2000</sub>-Nap 1% does not need to be injected via an intravitreal pathway to be found in the retina.

The AuNPs-PEG<sub>2000</sub>-Nap 1% are not the only AuNPs that were found in the retina after topical application (160). However, this phenomenon was previously demonstrated only in a mouse model, whose eye volume is approximately one hundred times smaller than that of a rabbit. Furthermore, *in vivo* biodistribution experiments benefit from having two possible routes for topically applied nanocarriers: the corneal and the non-corneal routes. Evidence also

suggests that the non-corneal route is beneficial in bringing more nanocarriers into the posterior segment of the eye (104, 161–164). However, according to the design of our *ex vivo* experiments, it is impossible for the AuNPs-PEG<sub>2000</sub>-Nap 1% to take a route other than the corneal route. Thus, future *in vivo* experiments will be able to highlight the duality of corneal and non-corneal routes in addition to validating which route is preferable for PEGylated AuNPs.

Following the previous observations made in the anterior segment, where AuNPs-PEG<sub>2000</sub>-Nap 1% were frequently found in the corneal epithelium, observed in the iris, and successfully located and retained in the monolayer of the lens epithelium, it is possible that AuNPs-PEG<sub>2000</sub>-Nap 1% may be also found in the RPE. This structure is a monolayer of pigmented cells forming part of the blood-retina barrier (165), which is heavily involved in the transport of ions, water, and metabolic waste from the subretinal space to the blood (166, 167), as well as the transport of nutrients from the blood to the photoreceptors (168, 169). In addition, RPE cells perform specialized phagocytosis, which is crucial in terms of maintaining the health of photoreceptors by digesting their aged outer segments. This process prevents photo-oxidative damage to photoreceptors (170). RPE cells do not divide; thus, they must process the ingested material efficiently to avoid toxic buildup in their lysosomes, which can lead to retinal disorders (171). This could be the reason why the AuNPs-PEG<sub>2000</sub>-Nap 1% were concentrated in this region of the posterior segment. This creates an extremely dynamic environment where AuNPs-PEG<sub>2000</sub>-Nap 1% could potentially be found, fitting the



description of tissues where they were observed in this study. However, further studies are required to investigate and confirm possibility.

## 4 Conclusion

In conclusion, AuNPs-PEG<sub>2000</sub>-Nap 1% were synthesized and exhibited similar properties as their nonfluorescent counterpart (AuNPs-PEG<sub>2000</sub>), e.g., ultrastability, low mucoadhesion, and low cytotoxicity, and they were internalized by the cells. When applied topically to *ex vivo* rabbit eyeballs, they demonstrated a strong affinity with the cornea, specifically the corneal epithelium. In addition, they were found in the iris, the lens epithelium, and the posterior segment of the eye. These results represent a tremendous opportunity for research on the potential of AuNPs as drug delivery systems.

The nanoparticle synthesis protocol developed in this study has the potential to be adapted for the creation of various types of AuNPs tailored to various applications and different target sites. This adaptability could be particularly beneficial for research focusing on the controlled release of active molecules in the cornea. By functionalizing the polymeric corona, it may be possible to increase

mucoadhesion, thereby improving the delivery and retention of therapeutic agents (101).

Previously, nonfluorescent AuNPs-PEG<sub>2000</sub> have demonstrated significant potential as drug carriers, particularly for delivering anti-inflammatory molecules (92). Building upon this foundation, future studies could investigate the encapsulation and release of active compounds designed to treat pathologies affecting the posterior segment of the eye. Such research could yield valuable insights and results, given that AuNPs can reach the back of the eye, thereby offering a promising delivery mechanism for drugs targeting this challenging area.

In this context, AuNPs have emerged as particularly promising candidates. For example, they have considerably potential for the targeted delivery of therapeutic molecules to the cornea, and they can reach the posterior segment of the eye. This dual functionality makes them an exciting prospect for future research, with the potential to advance the field of ocular drug delivery significantly. Thus, the continued investigation of their properties and applications could lead to new and more effective treatments for a range of eye conditions, benefiting patients with both anterior and posterior segment diseases.



## Data availability statement

The original contributions presented in the study are included in the article/[Supplementary material](#), further inquiries can be directed to the corresponding author.

## Ethics statement

Animal ethical approval was not required for the study involving animals in accordance with the local legislation and institutional requirements because albino rabbit heads were obtained from the Rolland Pouliot & Fils slaughterhouse (Saint-Henri-deLévis, QC, Canada). This study adhered to the ethical principles outlined in the Declaration of Helsinki and was approved by the CHU de Québec–Université Laval Ethics Committee (protocol number DR-002-955). The research-grade human eyes used in this study were provided by the “Ocular Tissue for Vision Research” infrastructure of the Vision Sciences Research Network, in collaboration with the Banque d’Yeux du Centre Universitaire d’Ophtalmologie (Québec, QC, Canada) and Héma-Québec (Québec, QC, Canada). The tissue acquisition process involved next-of-kin consent.

## Author contributions

GR-M: Conceptualization, Formal analysis, Methodology, Writing – original draft, Writing – review & editing. SM: Formal analysis, Methodology, Writing – review & editing. AT: Formal analysis, Methodology, Writing – review & editing. CB: Methodology, Writing – review & editing. CM: Methodology, Writing – review & editing. AL: Methodology, Writing – review & editing. SP: Funding acquisition, Resources, Supervision, Writing – review & editing. PR: Formal analysis, Resources, Supervision, Writing – review & editing. EG: Conceptualization, Formal analysis, Funding acquisition, Resources, Supervision, Writing – review & editing. EB: Conceptualization, Formal analysis, Funding acquisition, Project administration, Resources, Supervision, Writing – review & editing.

## Funding

The author(s) declare that financial support was received for the research and/or publication of this article. This work was funded by the Canadian Institutes of Health Research (CIHR), the Natural Sciences and Engineering Research Council of Canada, the Fondation du CHU de Québec, The Vision Health Research Network (VHRN), and the Fonds de Recherche du Québec-Nature et Technologie (FRQ-NT, Samuel de Champlain Grant in association with the Conseil Franco-Québécois de Coopération Universitaire (CFQCU)).

## References

- Land MF. The human eye: structure and function. *Nat Med.* (1999) 5:1229. doi: 10.1038/15713
- Baujat B, Krastinova D, Bach CA, Coquille F, Chabolle F. Orbital morphology in exophthalmos and Exorbitism. *Plast Reconstr Surg.* (2006) 117:542–50. doi: 10.1097/01.prs.0000200773.00268.56
- Gupta A, Kafetzis KN, Tagalakis AD, Yu-Wai-Man C. RNA therapeutics in ophthalmology - translation to clinical trials. *Exp Eye Res.* (2021) 205:108482. doi: 10.1016/j.exer.2021.108482
- Bucolo C, Drago F, Salomone S. Ocular drug delivery: a clue from nanotechnology. *Front Pharmacol.* (2012) 3:3. doi: 10.3389/fphar.2012.00188

Infrastructures were supported by grants from the Canadian Funds for Innovation.

## Acknowledgments

GRM acknowledges scholarships from Fonds de Recherche du Québec-Santé (FRQS), la Fondation du CHU de Québec-Desjardins, la Fondation des maladies de l’œil, and the VHRN. CM acknowledges scholarships from the Fondation des maladies de l’œil, the VHRN, and the Faculty of Medicine of Université Laval. AL acknowledges scholarship from CIHR. SP and PJR are Senior Research Scholars from the Fonds de Recherche du Québec-Santé (FRQ-S), and members of the Laboratoire d’Organogénèse Expérimentale (LOEX), and VHRN scientific networks. EB is a Junior 2 Research Scholar from the Fonds de Recherche du Québec-Santé (FRQ-S), and a member of the Centre de recherche sur les matériaux avancés (CERMA), Regroupement québécois de recherche sur la fonction, l’ingénierie et les applications des protéines (PROTEO), Centre québécois sur les matériaux fonctionnels (CQMF), and VHRN scientific networks.

## Conflict of interest

The authors declare that the research was conducted in the absence of any commercial or financial relationships that could be construed as a potential conflict of interest.

## Generative AI statement

The authors declare that no Gen AI was used in the creation of this manuscript.

## Publisher’s note

All claims expressed in this article are solely those of the authors and do not necessarily represent those of their affiliated organizations, or those of the publisher, the editors and the reviewers. Any product that may be evaluated in this article, or claim that may be made by its manufacturer, is not guaranteed or endorsed by the publisher.

## Supplementary material

The Supplementary material for this article can be found online at: <https://www.frontiersin.org/articles/10.3389/fmed.2025.1557611/full#supplementary-material>

5. Braun RJ, King-Smith PE, Begley CG, Li L, Gewecke NR. Dynamics and function of the tear film in relation to the blink cycle. *Prog Retin Eye Res.* (2015) 45:132–64. doi: 10.1016/j.preteyeres.2014.11.001
6. Herbaut A, Liang H, Denoyer A, Baudouin C, Labbé A. Tear film analysis and evaluation of optical quality: a review of the literature. *J Fr Ophthalmol.* (2019) 42:e21:–e35. doi: 10.1016/j.jfo.2018.12.001
7. McCulley JP, Shine WE. Meibomian gland function and the tear lipid layer. *Ocul Surf.* (2003) 1:97–106. doi: 10.1016/S1542-0124(12)70138-6
8. Portal C, Gouyer V, Gottrand F, Desseyn J-L. Ocular mucins in dry eye disease. *Exp Eye Res.* (2019) 186:107724. doi: 10.1016/j.exer.2019.107724
9. Dartt DA, Willcox MDP. Complexity of the tear film: importance in homeostasis and dysfunction during disease. *Exp Eye Res.* (2013) 117:1–3. doi: 10.1016/j.exer.2013.10.008
10. Bron AJ, Tiffany JM, Gouveia SM, Yokoi N, Voon LW. Functional aspects of the tear film lipid layer. *Exp Eye Res.* (2004) 78:347–60. doi: 10.1016/j.exer.2003.09.019
11. Castro-Balado A, Mondelo-García C, Zarra-Ferro I, Fernández-Ferreiro A. New ophthalmic drug delivery systems. *Farmacia Hospitalaria: Organo Oficial de Expresion Cientifica de la Sociedad Espanola de. Farm Hosp.* (2020) 44:149. doi: 10.7399/fh.11388
12. Mehuys E, Delaey C, Christiaens T, Van Bortel L, Van Tongelen I, Remon J-P, et al. Eye drop technique and patient-reported problems in a real-world population of eye drop users. *Eye.* (2020) 34:1392–8. doi: 10.1038/s41433-019-0665-y
13. Nayak K, Misra M. A review on recent drug delivery systems for posterior segment of eye. *Biomed Pharmacother.* (2018) 107:1564–82. doi: 10.1016/j.biopha.2018.08.138
14. Cabrera FJ, Wang DC, Reddy K, Acharya G, Shin CS. Challenges and opportunities for drug delivery to the posterior of the eye. *Drug Discov Today.* (2019) 24:1679–84. doi: 10.1016/j.drudis.2019.05.035
15. Ranta V-P, Mannermaa E, Lummeppuro K, Subrizi A, Laukkanen A, Antopolsky M, et al. Barrier analysis of periorcular drug delivery to the posterior segment. *J Control Release.* (2010) 148:42–8. doi: 10.1016/j.jconrel.2010.08.028
16. Nozaki M, Ando R, Kimura T, Kato F, Yasukawa T. The role of laser photocoagulation in treating diabetic macular edema in the era of intravitreal drug administration: a descriptive review. *Medicina.* (2023) 59:1319. doi: 10.3390/medicina59071319
17. Raizada K, Naik M. Photodynamic therapy for the eye. Treasure Island (FL): StatPearls Publishing (2023).
18. Campochiaro PA, Akhlaq A. Sustained suppression of VEGF for treatment of retinal/choroidal vascular diseases. *Prog Retin Eye Res.* (2021) 83:100921. doi: 10.1016/j.preteyeres.2020.100921
19. Seah I, Zhao X, Lin Q, Liu Z, Su SZZ, Yuen YS, et al. Use of biomaterials for sustained delivery of anti-VEGF to treat retinal diseases. *Eye.* (2020) 34:1341–56. doi: 10.1038/s41433-020-0770-y
20. Borrelli E, Grosso D, Barresi C, Lari G, Sacconi R, Senni C, et al. Long-term visual outcomes and morphologic biomarkers of vision loss in eyes with diabetic macular edema treated with anti-VEGF therapy. *Am J Ophthalmol.* (2022) 235:80–9. doi: 10.1016/j.ajo.2021.09.002
21. Tan Y, Fukutomi A, Sun MT, Durkin S, Gilhotra J, Chan WO. Anti-VEGF crunch syndrome in proliferative diabetic retinopathy: a review. *Surv Ophthalmol.* (2021) 66:926–32. doi: 10.1016/j.survophthal.2021.03.001
22. Foss A, Rotsos T, Empeslidis T, Chong V. Development of macular atrophy in patients with wet age-related macular degeneration receiving anti-VEGF treatment. *Ophthalmologica Journal International d'Ophthalmol Int J Ophthalmol Zeitschrift Fur Augenheilkunde.* (2022) 245:204–17. doi: 10.1159/000520171
23. Chatziralli I. Ranibizumab for the treatment of diabetic retinopathy. *Expert Opin Biol Ther.* (2021) 21:991–7. doi: 10.1080/14712598.2021.1928629
24. Bahar I, Kaiserman I, McAllum P, Rootman D, Slomovic A. Subconjunctival Bevacizumab Injection for Corneal Neovascularization. *Cornea.* (2008) 27:142–7. doi: 10.1097/ICO.0b013e318159019f
25. Ohr M, Kaiser PK. Intravitreal aflibercept injection for neovascular (wet) age-related macular degeneration. *Expert Opin Pharmacother.* (2012) 13:585–91. doi: 10.1517/14656566.2012.658368
26. Hussain RM, Hariprasad SM, Ciulla TA. Ophthalmic surgery, lasers and imaging. *Retina.* (2017) 48:780–4. doi: 10.3928/23258160-20170928-01
27. Ghasemi Falavarjani K, Nguyen QD. Adverse events and complications associated with intravitreal injection of anti-VEGF agents: a review of literature. *Eye.* (2013) 27:787–94. doi: 10.1038/eye.2013.107
28. Conlon R, Saheb H, Ahmed IIK. Canadian journal of ophthalmology. *J Canadien d'Ophthalmologie.* (2017) 52:114–24. doi: 10.1016/j.jcjo.2016.07.013
29. Mitchell P, Liew G, Gopinath B, Wong TY. Age-related macular degeneration. *Lancet.* (2018) 392:1147–59. doi: 10.1016/S0140-6736(18)31550-2
30. Mansour SE, Browning DJ, Wong K, Flynn HW Jr, Bhavsar AR. The evolving treatment of diabetic retinopathy. *Clin Ophthalmol.* (2020) 14:653–78. doi: 10.2147/OPTH.S236637
31. Sharma S. Diagnosis of infectious diseases of the eye. *Eye.* (2012) 26:177–84. doi: 10.1038/eye.2011.275
32. de Andrade FA, Fiorot SHS, Benchimol EI, Provenzano J, Martins VJ, Levy RA. The autoimmune diseases of the eyes. *Autoimmun Rev.* (2016) 15:258–71. doi: 10.1016/j.autrev.2015.12.001
33. Gautam M, Gupta R, Singh P, Verma V, Verma S, Mittal P, et al. Intracameral drug delivery: a review of agents, indications, and outcomes. *J Ocul Pharmacol Ther.* (2023) 39:102–16. doi: 10.1089/jop.2022.0144
34. Kim HM, Woo SJ. Ocular drug delivery to the retina: current innovations and future perspectives. *Pharmaceutics.* (2021) 13:13. doi: 10.3390/pharmaceutics13010108
35. Yavuz B, Pehlivan SB, Unlü N. Dendrimeric systems and their applications in ocular drug delivery. *TheScientificWorldJOURNAL.* (2013) 2013:732340. doi: 10.1155/2013/732340
36. Jünemann AGM, Chorągiewicz T, Ozimek M, Grieb P, Rejda R. Drug bioavailability from topically applied ocular drops. Does drop size matter? *Ophthalmology J.* (2016) 1:29–35. doi: 10.5603/OJ.2016.0005
37. Gaudana R, Ananthula HK, Parenky A, Mitra AK. Ocular drug delivery. *AAPS J.* (2010) 12:348–60. doi: 10.1208/s12248-010-9183-3
38. Honda M, Asai T, Oku N, Araki Y, Tanaka M, Ebihara N. Liposomes and nanotechnology in drug development: focus on ocular targets. *Int J Nanomedicine.* (2013) 8:495. doi: 10.2147/IJN.S30725
39. Yasukawa T, Ogura Y, Tabata Y, Kimura H, Wiedemann P, Honda Y. Drug delivery systems for vitreoretinal diseases. *Prog Retin Eye Res.* (2004) 23:253–81. doi: 10.1016/j.preteyeres.2004.02.003
40. Ranch K, Chawnani D, Jani H, Acharya D, Patel CA, Jacob S, et al. An update on the latest strategies in retinal drug delivery. *Expert Opin Drug Deliv.* (2024) 21:695–712. doi: 10.1080/17425247.2024.2358886
41. Wang R, Gao Y, Liu A, Zhai G. A review of nanocarrier-mediated drug delivery systems for posterior segment eye disease: challenges analysis and recent advances. *J Drug Target.* (2021) 29:687–702. doi: 10.1080/1061186X.2021.1878366
42. Meza-Rios A, Navarro-Partida J, Armendariz-Borunda J, Santos A. Therapies based on nanoparticles for eye drug delivery. *Ophthalmol Therapy.* (2020) 9:1–14. doi: 10.1007/s40123-020-00257-7
43. Jumelle C, Gholizadeh S, Annabi N, Dana R. Advances and limitations of drug delivery systems formulated as eye drops. *J Control Release.* (2020) 321:1–22. doi: 10.1016/j.jconrel.2020.01.057
44. Bonilla L, Espina M, Severino P, Cano A, Ettcheto M, Camins A, et al. Lipid nanoparticles for the posterior eye segment. *Pharmaceutics.* (2022) 14:90. doi: 10.3390/pharmaceutics14010090
45. Baig MS, Karade SK, Ahmad A, Khan MA, Haque A, Webster TJ, et al. Lipid-based nanoparticles: innovations in ocular drug delivery. *Front Mol Biosci.* (2024) 11:11. doi: 10.3389/fmolb.2024.1421959
46. Tsung T-H, Tsai Y-C, Lee H-P, Chen Y-H, Lu D-W. Biodegradable polymer-based drug-delivery Systems for Ocular Diseases. *Int J Mol Sci.* (2023) 24:12976. doi: 10.3390/ijms241612976
47. Biswas A, Choudhury AD, Bisen AC, Agrawal S, Sanap SN, Verma SK, et al. Trends in formulation approaches for sustained drug delivery to the posterior segment of the eye. *AAPS PharmSciTech.* (2023) 24:217. doi: 10.1208/s12249-023-02673-x
48. Bhandari M, Nguyen S, Yazdani M, Utheim TP, Hagesaether E. The therapeutic benefits of Nanoencapsulation in drug delivery to the anterior segment of the eye: a systematic review. *Front Pharmacol.* (2022) 13:13. doi: 10.3389/fphar.2022.903519
49. Vaneev A, Tikhomirova V, Chesnokova N, Popova E, Beznos O, Kost O, et al. Nanotechnology for topical drug delivery to the anterior segment of the eye. *Int J Mol Sci.* (2021) 22:12368. doi: 10.3390/ijms222212368
50. Li Q, Weng J, Wong SN, Thomas Lee WY, Chow SF. Nanoparticulate drug delivery to the retina. *Mol Pharm.* (2021) 18:506–21. doi: 10.1021/acs.molpharmaceut.0c00224
51. Shafiq M, Rafique M, Cui Y, Pan L, Do C-W, Ho EA. An insight on ophthalmic drug delivery systems: focus on polymeric biomaterials-based carriers. *J Control Release.* (2023) 362:446–67. doi: 10.1016/j.jconrel.2023.08.041
52. Akhter MH, Ahmad I, Alshahrani MY, Al-Harbi AI, Khalilullah H, Afzal O, et al. Drug delivery challenges and current Progress in Nanocarrier-based ocular therapeutic system. *Gels.* (2022) 8:82. doi: 10.3390/gels8020082
53. Zhang T, Jin X, Zhang N, Jiao X, Ma Y, Liu R, et al. Targeted drug delivery vehicles mediated by nanocarriers and aptamers for posterior eye disease therapeutics: barriers, recent advances and potential opportunities. *Nanotechnology.* (2022) 33:162001. doi: 10.1088/1361-6528/ac46d5
54. Mobaraki M, Soltani M, Zare Harofte S, Zoudani EL, Daliri R, Aghamirsalim M, et al. Biodegradable nanoparticle for cornea drug delivery: focus review. *Pharmaceutics.* (2020) 12:1232. doi: 10.3390/pharmaceutics12121232
55. Yang Y, Lockwood A. Topical ocular drug delivery systems: innovations for an unmet need. *Exp Eye Res.* (2022) 218:109006. doi: 10.1016/j.exer.2022.109006
56. Tawfik M, Chen F, Goldberg JL, Sabel BA. Nanomedicine and drug delivery to the retina: current status and implications for gene therapy. *Naunyn Schmiedeberg's Arch Pharmacol.* (2022) 395:1477–507. doi: 10.1007/s00210-022-02287-3

57. Khiev D, Mohamed ZA, Vichare R, Paulson R, Bhatia S, Mohapatra S, et al. Emerging Nano-formulations and nanomedicines applications for ocular drug delivery. *Nano*. (2021) 11:173. doi: 10.3390/nano11010173
58. Chaudhari P, Lewis SA, Ghathe V. Nanotechnology-based non-invasive strategies in ocular therapeutics: approaches, limitations to clinical translation, and safety concerns. *Contact Lens and Anterior Eye*. (2025):102367. doi: 10.1016/j.clae.2025.102367
59. Kim JH, Kim JH, Kim K-W, Kim MH, Yu YS. Intravenously administered gold nanoparticles pass through the blood-retinal barrier depending on the particle size, and induce no retinal toxicity. *Nanotechnology*. (2009) 20:505101. doi: 10.1088/0957-4484/20/50/505101
60. Singh R, Batoki JC, Ali M, Bonilha VL, Anand-Apte B. Nanomedicine: nanotechnology. *Biol Med*. (2020) 28:102205. doi: 10.1016/j.nano.2020.102205
61. Sun Y-N, Wang C-D, Zhang X-M, Ren L, Tian X-H. Shape dependence of gold nanoparticles on In Vivo Acute toxicological effects and biodistribution. *J Nanosci Nanotechnol*. (2011) 11:1210–6. doi: 10.1166/jnn.2011.3094
62. Kim JH, Kim MH, Jo DH, Yu YS, Lee TG, Kim JH. The inhibition of retinal neovascularization by gold nanoparticles via suppression of VEGFR-2 activation. *Biomaterials*. (1865) 32:1865–71. doi: 10.1016/j.biomaterials.2010.11.030
63. Bakri SJ, Pulido JS, Mukherjee P, Marler RJ, Mukhopadhyay D. Absence of histologic retinal toxicity of intravitreal NANOGOLD in a rabbit model. *Retina*. (2008) 28:147–9. doi: 10.1097/IAE.0b013e3180dc9360
64. Luo L-J, Jian H-J, Harroun SG, Lai J-Y, Unnikrishnan B, Huang C-C. Targeting nanocomposites with anti-oxidative/inflammatory/angiogenic activities for synergistically alleviating macular degeneration. *Appl Mater Today*. (2021) 24:101156. doi: 10.1016/j.apmt.2021.101156
65. Jo DH, Kim JH, Son JG, Piao Y, Lee TG, Kim JH. Inhibitory activity of gold and silica nanoparticles to vascular endothelial growth factor (VEGF)-mediated angiogenesis is determined by their sizes. *Nano Res*. (2014) 7:844–52. doi: 10.1007/s12274-014-0445-8
66. Hayashi A, Naseri A, Pennesi ME, de Juan E. Subretinal delivery of immunoglobulin G with gold nanoparticles in the rabbit eye. *Jpn J Ophthalmol*. (2009) 53:249–56. doi: 10.1007/s10384-009-0655-x
67. Dong Y, Wan G, Yan P, Qian C, Li F, Peng G. Fabrication of resveratrol coated gold nanoparticles and investigation of their effect on diabetic retinopathy in streptozotocin induced diabetic rats. *J Photochem Photobiol B Biol*. (2019) 195:51–7. doi: 10.1016/j.jphotobiol.2019.04.012
68. Karthikeyan B, Kalishwaral K, Sheikpranbabu S, Deepak V, Haribalaganesh R, Gurunathan S. Gold nanoparticles downregulate VEGF and IL-1 $\beta$ -induced cell proliferation through Src kinase in retinal pigment epithelial cells. *Exp Eye Res*. (2010) 91:769–78. doi: 10.1016/j.exer.2010.09.003
69. Karakoçak BB, Raliya R, Plassid JM, Chavalmane S, Wang W-N, Ravi N, et al. Biocompatibility of gold nanoparticles in retinal pigment epithelial cell line. *Toxicol in Vitro*. (2016) 37:61–9. doi: 10.1016/j.tiv.2016.08.013
70. Wang Y, Xia R, Hu H, Peng T. Biosynthesis, characterization and cytotoxicity of gold nanoparticles and their loading with N-acetylcarnosine for cataract treatment. *J Photochem Photobiol B Biol*. (2018) 187:180–3. doi: 10.1016/j.jphotobiol.2018.08.014
71. Mitra M, Kandalam M, Rangasamy J, Shankar B, Maheswari UK, Swaminathan S, et al. Molecular vision (2013) 19:1029.
72. Trigueros S, Domènech EB, Toulis V, Marfany G. In vitro gene delivery in retinal pigment epithelium cells by plasmid DNA-wrapped gold nanoparticles. *Gen Dent*. (2019) 10:289. doi: 10.3390/genes10040289
73. Apaolaza PS, Busch M, Asin-Prieto E, Peynshaert K, Rathod R, Remaut K, et al. Hyaluronic acid coating of gold nanoparticles for intraocular drug delivery: evaluation of the surface properties and effect on their distribution. *Exp Eye Res*. (2020) 198:108151. doi: 10.1016/j.exer.2020.108151
74. Maulvi FA, Patil RJ, Desai AR, Shukla MR, Vaidya RJ, Ranch KM, et al. Effect of gold nanoparticles on timolol uptake and its release kinetics from contact lenses: in vitro and in vivo evaluation. *Acta Biomater*. (2019) 86:350–62. doi: 10.1016/j.actbio.2019.01.004
75. Li Q, Ma C, Ma Y, Ma Y, Mao Y, Meng Z. Journal of biomaterials science. *Polymer Edition*. (2021) 32:1618–34. doi: 10.1080/09205063.2021.1927656
76. Guo Q, Jia L, Qinggeletu R, Zhang XY. In vitro and in vivo evaluation of ketotifen-gold nanoparticles laden contact lens for controlled drug delivery to manage conjunctivitis. *J Drug Delivery Sci Technol*. (2021) 64:102538. doi: 10.1016/j.jddst.2021.102538
77. Salem HF, Ahmed SM, Omar MM. Liposomal flucytosine capped with gold nanoparticle formulations for improved ocular delivery. *Drug Des Devel Ther*. (2016) 10:277. doi: 10.2147/DDDT.S91730
78. Pereira DV, Petronilho F, Pereira HRSB, Vuolo F, Mina F, Possato JC, et al. Effects of gold nanoparticles on endotoxin-induced uveitis in rats. *Invest Ophthalmol Vis Sci*. (2012) 53:8036. doi: 10.1167/iovs.12-10743
79. Sharma A, Tandon A, Tovey JCK, Gupta R, Robertson JD, Fortune JA, et al. Nanomedicine: nanotechnology. *Biol Med*. (2011) 7:505–13. doi: 10.1016/j.nano.2011.01.006
80. Tandon A, Sharma A, Rodier JT, Klivanov AM, Rieger FG, Mohan RR. BMP7 gene transfer via gold nanoparticles into stroma inhibits corneal fibrosis in vivo. *PLoS One*. (2013) 8:e66434. doi: 10.1371/journal.pone.0066434
81. Neves J d, Bahia MF, Amiji MM, Sarmiento B. Mucoadhesive nanomedicines: characterization and modulation of mucoadhesion at the nanoscale. *Expert Opin Drug Deliv*. (2011) 8:1085–104. doi: 10.1517/17425247.2011.586334
82. Hock N, Racaniello GF, Aspinnall S, Denora N, Khutoryanskiy VV, Bernkop-Schnürch A. Thiolated nanoparticles for biomedical applications: mimicking the workhorses of our body. *Advan Sci*. (2022) 9:e2102451. doi: 10.1002/advs.202102451
83. Yeh Y-C, Creran B, Rotello VM. Gold nanoparticles: preparation, properties, and applications in bionanotechnology. *Nanoscale*. (1871) 4:1871–80. doi: 10.1039/C1NR11188D
84. Alex S, Tiwari A. Functionalized gold nanoparticles: synthesis, properties and applications—a review. *J Nanosci Nanotechnol*. (1869) 15:1869–94. doi: 10.1166/jnn.2015.9718
85. Bansal SA, Kumar V, Karimi J, Singh AP, Kumar S. Role of gold nanoparticles in advanced biomedical applications. *Nanoscale Advan*. (2020) 2:3764–87. doi: 10.1039/D0NA00472C
86. Cabuzu D, Cirja A, Puiu R, Grumezescu AM. Biomedical applications of gold nanoparticles. *Curr Top Med Chem*. (2015) 15:1605–13. doi: 10.2174/1568026615666150414144750
87. Cordeiro M, Ferreira Carlos FF, Pedrosa P, Lopez A, Baptista PV. Gold nanoparticles for diagnostics: advances towards points of care. *Diagnostics*. (2016) 6:6. doi: 10.3390/diagnostics6040043
88. Kong F-Y, Zhang J-W, Li R-F, Wang Z-X, Wang W-J, Wang W. Unique roles of gold nanoparticles in drug delivery, targeting and imaging applications. *Molecules*. (2017) 22:22. doi: 10.3390/molecules22091445
89. Marangoni VS, Cancino-Bernardi J, Zucolotto V. Synthesis, Physico-chemical properties, and biomedical applications of gold Nanorods—a review. *J Biomed Nanotechnol*. (2016) 12:1136–58. doi: 10.1166/jbn.2016.2218
90. Masse F, Desjardins P, Ouellette M, Couture C, Omar MM, Pernet V, et al. Synthesis of Ultrastable gold nanoparticles as a new drug delivery system. *Molecules*. (2019) 24:24. doi: 10.3390/molecules24162929
91. Masse F, Ouellette M, Lamoureux G, Boisselier E. Gold nanoparticles in ophthalmology. *Med Res Rev*. (2019) 39:302–27. doi: 10.1002/med.21509
92. Raiche-Marcoux G, Loiseau A, Maranda C, Poliquin A, Boisselier E. Parametric drug release optimization of anti-inflammatory drugs by gold nanoparticles for topically applied ocular therapy. *Int J Mol Sci*. (2022) 23:23. doi: 10.3390/ijms232416191
93. Gaudreault M, Carrier P, Larouche K, Leclerc S, Giasson M, Germain L, et al. Influence of Sp1/Sp3 expression on corneal epithelial cells proliferation and differentiation properties in reconstructed tissues. *Investig Ophthalmol Vis Sci*. (2003) 44:1447. doi: 10.1167/iovs.02-0707
94. Germain L, Auger FA, Grandbois E, Guignard R, Giasson M, Boisjoly H, et al. Pathobiology: journal of immunopathology. *Mol Cell Biol*. (1999) 67:140–7. doi: 10.1159/000028064
95. Bisson F, Rochefort E, Lavoie A, Larouche D, Zaniolo K, Simard-Bisson C, et al. Irradiated human dermal fibroblasts are as efficient as mouse fibroblasts as a feeder layer to improve human epidermal cell culture lifespan. *Int J Mol Sci*. (2013) 14:4684–704. doi: 10.3390/ijms14034684
96. Le-Bel G, Giasson CJ, Deschambeault A, Carrier P, Germain L, Guérin SL. The presence of a feeder layer improves human corneal endothelial cell proliferation by altering the expression of the transcription factors Sp1 and NF1. *Exp Eye Res*. (2018) 176:161–73. doi: 10.1016/j.exer.2018.07.009
97. Montoya IA, Pluth MD. Selective turn-on fluorescent probes for imaging hydrogen sulfide in living cells. *Chem Commun*. (2012) 48:4767–9. doi: 10.1039/c2cc30730h
98. Loiseau A, Zhang L, Hu D, Salmain M, Mazouzi Y, Flack R, et al. Core-Shell gold/silver nanoparticles for localized surface Plasmon resonance-based naked-eye toxin biosensing. *ACS Appl Mater Interfaces*. (2019) 11:46462–71. doi: 10.1021/acsami.9b14980
99. Chen P, Liedberg B. Curvature of the localized surface Plasmon resonance peak. *Anal Chem*. (2014) 86:7399–405. doi: 10.1021/ac500883x
100. Chen P, Tran NT, Wen X, Xiong Q, Liedberg B. Inflection point of the localized surface Plasmon resonance peak: a general method to improve the sensitivity. *ACS Sensors*. (2017) 2:235–42. doi: 10.1021/acssensors.6b00633
101. Ouellette M, Masse F, Lefebvre-Demers M, Maestracchi Q, Grenier P, Millar R, et al. Insights into gold nanoparticles as a mucoadhesive system. *Sci Rep*. (2018) 8:14357. doi: 10.1038/s41598-018-32699-2
102. Onugwu AL, Nwagwu CS, Onugwu OS, Echezona AC, Agbo CP, Ihim SA, et al. Nanotechnology based drug delivery systems for the treatment of anterior segment eye diseases. *J Control Release*. (2023) 354:465–88. doi: 10.1016/j.jconrel.2023.01.018
103. Zimmer A, Kreuter J. Microspheres and nanoparticles used in ocular delivery systems. *Adv Drug Deliv Rev*. (1995) 16:61–73. doi: 10.1016/0169-409X(95)00017-2
104. Hironaka K, Inokuchi Y, Tozuka Y, Shimazawa M, Hara H, Takeuchi H. Design and evaluation of a liposomal delivery system targeting the posterior segment of the eye. *J Control Release*. (2009) 136:247–53. doi: 10.1016/j.jconrel.2009.02.020
105. Alvarez-Trabado J, Diebold Y, Sanchez A. Designing lipid nanoparticles for topical ocular drug delivery. *Int J Pharm*. (2017) 532:204–17. doi: 10.1016/j.ijpharm.2017.09.017

106. Lai SK, Wang Y-Y, Hanes J. Mucus-penetrating nanoparticles for drug and gene delivery to mucosal tissues. *Adv Drug Deliv Rev.* (2009) 61:158–71. doi: 10.1016/j.addr.2008.11.002
107. Toropainen E, Fraser-Miller SJ, Novakovic D, Del Amo EM, Vellonen K-S, Ruponen M, et al. Biopharmaceutics of topical ophthalmic suspensions: importance of viscosity and particle size in ocular absorption of indomethacin. *Pharmaceutics.* (2021) 13:452. doi: 10.3390/pharmaceutics13040452
108. Jo DH, Kim JH, Lee TG, Kim JH. Nanomedicine: Nanotechnology. *Biol Med.* (2015) 11:1603–11. doi: 10.1016/j.nano.2015.04.015
109. Mahaling B, Katti DS. Understanding the influence of surface properties of nanoparticles and penetration enhancers for improving bioavailability in eye tissues in vivo. *Int J Pharm.* (2016) 501:1–9. doi: 10.1016/j.ijpharm.2016.01.053
110. Mahaling B, Katti DS. Nanomedicine: Nanotechnology. *Biol Med.* (2016) 12:2149–60. doi: 10.1016/j.nano.2016.05.017
111. Reznickova A, Slavikova N, Kolska Z, Kolarova K, Belinova T, Hubalek Kalbacova M, et al. PEGylated gold nanoparticles: stability, cytotoxicity and antibacterial activity. *Colloids Surf A Physicochem Eng Asp.* (2019) 560:26–34. doi: 10.1016/j.colsurfa.2018.09.083
112. Henson JC, Brickell A, Kim J-W, Jensen H, Mehta JL, Jensen M. PEGylated gold nanoparticle toxicity in cardiomyocytes: assessment of size, concentration, and time dependency. *IEEE Trans Nanobiosci.* (2022) 21:387–94. doi: 10.1109/TNB.2022.3154438
113. Sasaki A. Recent advances in the standardization of fluorescence microscopy for quantitative image analysis. *Biophys Rev.* (2022) 14:33–9. doi: 10.1007/s12551-021-00871-0
114. Hickey SM, Ung B, Bader C, Brooks R, Lazniewska J, Johnson IRD, et al. Fluorescence microscopy—an outline of hardware, biological handling, and fluorophore considerations. *Cells.* (2022) 11:35. doi: 10.3390/cells11010035
115. Fan J, Cheng Y, Sun M. Functionalized gold nanoparticles: synthesis, properties and biomedical applications. *Chem Rec.* (2020) 20:1474–504. doi: 10.1002/tcr.202000087
116. Chatterjee S, Lou X-Y, Liang F, Yang Y-W. Surface-functionalized gold and silver nanoparticles for colorimetric and fluorescent sensing of metal ions and biomolecules. *Coord Chem Rev.* (2022) 459:214461. doi: 10.1016/j.ccr.2022.214461
117. Boisselier E, Salmon L, Ruiz J, Astruc D. How to very efficiently functionalize gold nanoparticles by “click” chemistry. *Chem Commun.* (2008):5788. doi: 10.1039/b812249k
118. Le Droumaguet C, Wang C, Wang Q. Fluorogenic click reaction. *Chem Soc Rev.* (2010) 39:1233–9. doi: 10.1039/B901975H
119. Perala SRK, Kumar S. On the mechanism of metal nanoparticle synthesis in the Brust–Schiffrin method. *Langmuir: ACS J Surfaces and Colloids.* (2013) 29:9863–73. doi: 10.1021/la401604q
120. Lu Y, Chen W In: DMP Mingos, editor. Gold clusters, colloids and nanoparticles I. Berlin: Springer International Publishing (2014). 117.
121. Rubinson KA, Krueger S. Poly(ethylene glycol)s 2000–8000 in water may be planar: a small-angle neutron scattering (SANS) structure study. *Polymer.* (2009) 50:4852–8. doi: 10.1016/j.polymer.2009.08.023
122. Pai SS, Hammouda B, Hong K, Pozzo DC, Przybycien TM, Tilton RD. The conformation of the poly(ethylene glycol) chain in mono-PEGylated lysozyme and mono-PEGylated human growth hormone. *Bioconjug Chem.* (2011) 22:2317–23. doi: 10.1021/bc2003583
123. Liu D, Li P-Y, Wang S-J, Gong B, Lu T, Li G-Y. *Spectrochimica Acta. Part A, Molecular and Biomolecular Spectroscopy.* (2022) 271:120872. doi: 10.1016/j.saa.2022.120872
124. Stewart DJ, Dalton MJ, Long SL, Kannan R, Yu Z, Cooper TM, et al. Steric hindrance inhibits excited-state relaxation and lowers the extent of intramolecular charge transfer in two-photon absorbing dyes. *Physical Chem Chem Physics: PCCP.* (2016) 18:5587–96. doi: 10.1039/C5CP07716H
125. Lyu Y, Becerril LM, Vanzan M, Corni S, Cattelan M, Granozzi G, et al. The interaction of amines with gold nanoparticles. *Adv Mater.* (2024) 36:2211624. doi: 10.1002/adma.202211624
126. Qi J, Hu X, Dong X, Lu Y, Lu H, Zhao W, et al. Towards more accurate bioimaging of drug nanocarriers: turning aggregation-caused quenching into a useful tool. *Adv Drug Deliv Rev.* (2019) 143:206–25. doi: 10.1016/j.addr.2019.05.009
127. Phan HT, Haes AJ. What does nanoparticle stability mean? *J Phys Chem C.* (2019) 123:16495–507. doi: 10.1021/acs.jpcc.9b00913
128. Amina SJ, Guo B. A review on the synthesis and functionalization of gold nanoparticles as a drug delivery vehicle. *Int J Nanomedicine.* (2020) 15:9823–57. doi: 10.2147/IJN.S279094
129. Pissuwan D, Niidome T, Cortie MB. The forthcoming applications of gold nanoparticles in drug and gene delivery systems. *J Control Release.* (2011) 149:65–71. doi: 10.1016/j.jconrel.2009.12.006
130. Chen PC, Mwakwari SC, Oyeler AK. Nanotechnology. *Sci Applic.* (2008) 1:45–66. doi: 10.2147/NSA.S3707
131. Wu Y, Ali MRK, Chen K, Fang N, El-Sayed MA. Gold nanoparticles in biological optical imaging. *Nano Today.* (2019) 24:120–40. doi: 10.1016/j.nantod.2018.12.006
132. Sun M, Liu F, Zhu Y, Wang W, Hu J, Liu J, et al. Salt-induced aggregation of gold nanoparticles for photoacoustic imaging and photothermal therapy of cancer. *Nanoscale.* (2016) 8:4452–7. doi: 10.1039/C6NR00056H
133. Zhang M, Shao S, Yue H, Wang X, Zhang W, Chen F, et al. High stability au NPs: from design to application in nanomedicine. *Int J Nanomedicine.* (2021) 16:6067–94. doi: 10.2147/IJN.S322900
134. Kyriakides TR, Raj A, Tseng TH, Xiao H, Nguyen R, Mohammed FS, et al. Biocompatibility of nanomaterials and their immunological properties. *Biomed Mater.* (2021) 16:042005. doi: 10.1088/1748-605X/abe5fa
135. Martínez R, Navarro Poupard M. F., Álvarez A., Soprano E., Migliavacca M. in Nanoparticles for biomedical applications (Eds.: E. J. Chung, L. Leon and C. Rinaldi), Elsevier, Ch. 2, London, (2020), pp. 5.
136. Xavier J, Vincent S, Meder F, Vollmer F. Advances in optoplasmonic sensors – combining optical nano/microcavities and photonic crystals with plasmonic nanostructures and nanoparticles. *Nano.* (2018) 7:1–38. doi: 10.1515/nanoph-2017-0064
137. Arcas AS, Jaramillo L, Costa NS, Allil RCSB, Werneck MM. Localized surface plasmon resonance-based biosensor on gold nanoparticles for *Taenia solium* detection. *Appl Opt.* (2021) 60:8137. doi: 10.1364/AO.432990
138. Bansil R, Turner BS. Mucin structure, aggregation, physiological functions and biomedical applications. *Curr Opin Colloid Interface Sci.* (2006) 11:164–70. doi: 10.1016/j.cocis.2005.11.001
139. Mackie AR, Goycoolea FM, Menchicchi B, Caramella CM, Saporito F, Lee S, et al. Innovative methods and applications in Mucoadhesion research. *Macromol Biosci.* (2017) 17:1600534. doi: 10.1002/mabi.201600534
140. Corfield AP. *Biochimica et Biophysica Acta (BBA). General Subjects.* (2015) 1850:236–52. doi: 10.1016/j.bbagen.2014.05.003
141. Hori Y. Secreted mucins on the ocular surface. *Investig Ophthalmol Vis Sci.* (2018) 59:DES151. doi: 10.1167/iovs.17-23623
142. Ludwig A. The use of mucoadhesive polymers in ocular drug delivery. *Adv Drug Deliv Rev.* (2005) 57:1595–639. doi: 10.1016/j.addr.2005.07.005
143. Mantle M, Allen A. A colorimetric assay for glycoproteins based on the periodic acid/Schiff stain. *Biochem Soc Trans.* (1978) 6:607–9. doi: 10.1042/bst0060607
144. Robins JH, Abrams GD, Pincock JA. The structure of Schiff reagent aldehyde adducts and the mechanism of the Schiff reaction as determined by nuclear magnetic resonance spectroscopy. *Can J Chem.* (1980) 58:339–47. doi: 10.1139/v80-055
145. Guo Y, Ma Y, Chen X, Li M, Ma X, Cheng G, et al. Mucus penetration of surface-engineered nanoparticles in various pH microenvironments. *ACS Nano.* (2023) 17:2813–28. doi: 10.1021/acsnano.2c11147
146. Rodrigues GA, Lutz D, Shen J, Yuan X, Shen H, Cunningham J, et al. Topical drug delivery to the posterior segment of the eye: addressing the challenge of preclinical to clinical translation. *Pharm Res.* (2018) 35:245. doi: 10.1007/s11095-018-2519-x
147. Loiseau A, Raiche-Marcoux G, Maranda C, Bertrand N, Boisselier E. Animal models in eye research: focus on corneal pathologies. *Int J Mol Sci.* (2023) 24:16661. doi: 10.3390/ijms242316661
148. Shen J, Durairaj C, Lin T, Liu Y, Burke J. Ocular pharmacokinetics of intravitreally administered Brimonidide and dexamethasone in animal models with and without blood–retinal barrier breakdown. *Invest Ophthalmol Vis Sci.* (2014) 55:1056. doi: 10.1167/iovs.13-13650
149. Hung KH, Yeh LK. Ex Vivo and In Vivo Animal Models for mechanical and chemical injuries of corneal epithelium. *J Vis Exp.* (2022) 182:e63217. doi: 10.3791/63217
150. Mascolini MV, Toniolo I, Carniel EL, Fontanella CG. Ex vivo, in vivo and in silico studies of corneal biomechanics: a systematic review. *Physical Eng Sci Med.* (2024) 47:403–41. doi: 10.1007/s13246-024-01403-2
151. Stradleigh TW, Ishida AT. Fixation strategies for retinal immunohistochemistry. *Prog Retin Eye Res.* (2015) 48:181–202. doi: 10.1016/j.preteyeres.2015.04.001
152. Espana EM, Birk DE. Composition, structure and function of the corneal stroma. *Exp Eye Res.* (2020) 198:108137. doi: 10.1016/j.exer.2020.108137
153. Yang H, Yu PK, Cringle SJ, Sun X, Yu D-Y. Iridal vasculature and the vital roles of the iris. *J Nat Sci.* (2015) 1:157.
154. Stauss HM, Rarick KR, Leick KM, Burkle JW, Rotella DL, Anderson MG. American journal of physiology. *Regulatory, Integrative Comparative Physiol.* (2011) 300:R1333–43. doi: 10.1152/ajpregu.00561.2010
155. Bloemendal H, de Jong W, Jaenicke R, Lubsen NH, Slingsby C, Tardieu A. Ageing and vision: structure, stability and function of lens crystallins. *Prog Biophys Mol Biol.* (2004) 86:407–85. doi: 10.1016/j.pbiomolbio.2003.11.012
156. Hendrickson A. Development of retinal layers in prenatal human retina. *Am J Ophthalmol.* (2016) 161:29–35.e1. doi: 10.1016/j.ajo.2015.09.023
157. Rajendran Nair DS, Seiler MJ, Patel KH, Thomas V, Martinez Camarillo JC, Humayun MS, et al. Tissue engineering strategies for retina regeneration. *Appl Sci.* (2021) 11:2154. doi: 10.3390/app11052154
158. Masland RH. The fundamental plan of the retina. *Nat Neurosci.* (2001) 4:877–86. doi: 10.1038/nn0901-877

159. Le Goff MM, Bishop PN. Adult vitreous structure and postnatal changes. *Eye*. (2008) 22:1214–22. doi: 10.1038/eye.2008.21
160. Laradji A, Karakocak BB, Kolesnikov AV, Kefalov VJ, Ravi N. Hyaluronic acid-based gold nanoparticles for the topical delivery of therapeutics to the retina and the retinal pigment epithelium. *Polymers*. (2021) 13:3324. doi: 10.3390/polym13193324
161. Puglia C, Santonocito D, Romeo G, Intagliata S, Romano GL, Stretto E, et al. Lipid nanoparticles traverse non-corneal path to reach the posterior eye segment: in vivo evidence. *Molecules*. (2021) 26:4673. doi: 10.3390/molecules26154673
162. Qi Q, Wei Y, Zhang X, Guan J, Mao S. Challenges and strategies for ocular posterior diseases therapy via non-invasive advanced drug delivery. *J Control Release*. (2023) 361:191–211. doi: 10.1016/j.jconrel.2023.07.055
163. Hughes PM, Olejnik O, Chang-Lin JE, Wilson CG. Topical and systemic drug delivery to the posterior segments. *Adv Drug Deliv Rev*. (2010) 57:2010–32. doi: 10.1016/j.addr.2005.09.004
164. Gu Y, Xu C, Wang Y, Zhou X, Fang L, Cao F. Multifunctional nanocomposites based on liposomes and layered double hydroxides conjugated with Glycylsarcosine for efficient topical drug delivery to the posterior segment of the eye. *Mol Pharm*. (2019) 16:2845–57. doi: 10.1021/acs.molpharmaceut.8b01136
165. Bok D. The retinal pigment epithelium: a versatile partner in vision. *J Cell Sci*. (1993) 1993:189–95. doi: 10.1242/jcs.1993.Supplement\_17.27
166. Boulton M, Dayhaw-Barker P. The role of the retinal pigment epithelium: topographical variation and ageing changes. *Eye*. (2001) 15:384–9. doi: 10.1038/eye.2001.141
167. Hamann S. International review of cytology, vol. 215. United States: Academic Press (2002). 395 p. Available at: <https://www.biblio.com/book/international-review-cytology-vol-215-survey/d/1548311742>
168. Besch D, Jägle H, Scholl HPN, Seeliger MW, Zrenner E. Inherited multifocal RPE-diseases: mechanisms for local dysfunction in global retinoid cycle gene defects. *Vis Res*. (2003) 43:3095–108. doi: 10.1016/j.visres.2003.09.020
169. Strauss O. The retinal pigment epithelium in visual function. *Physiol Rev*. (2005) 85:845–81. doi: 10.1152/physrev.00021.2004
170. Valiente-Soriano FJ, Salinas-Navarro M, Di Pierdomenico J, García-Ayuso D, Lucas-Ruiz F, Pinilla I, et al. Tracing the retina to analyze the integrity and phagocytic capacity of the retinal pigment epithelium. *Sci Rep*. (2020) 10:7273. doi: 10.1038/s41598-020-64131-z
171. Kwon W, Freeman SA. Phagocytosis by the retinal pigment epithelium: recognition, resolution, recycling. *Front Immunol*. (2020) 11:11. doi: 10.3389/fimmu.2020.604205